MICROFLUIDIC DROP FORMATION WITH POLYMER PLASTICS

by

Shu-Che Peng

B. S. in Chemical Engineering, National Cheng Kung University, Taiwan, 2008

Submitted to the Graduate Faculty of

Swanson School of Engineering in partial fulfillment

of the requirements for the degree of

Master of Science

University of Pittsburgh

2012

UNIVERSITY OF PITTSBURGH

SWANSON SCHOOL OF ENGINEERING

This thesis was presented

by

Shu-Che Peng

It was defended on

June 1, 2012

and approved by

Sachin Velankar, PhD, Associate Professor, Department of Chemical and Petroleum Engineering

Joseph J. McCarthy, PhD, Associate Professor, Department of Chemical and Petroleum Engineering

Robert M Enick, PhD, Professor, Department of Chemical and Petroleum Engineering

Thesis Advisor: Sachin Velankar, PhD, Associate Professor, Department of Chemical and Petroleum Engineering

MICROFLUIDIC DROP FORMATION WITH POLYMER PLASTICS

Shu-Che Peng, M.S.

University of Pittsburgh, 2012

The aim of this study is to develop a microfluidic platform for making particles from molten polymers. This thesis describes the process of formation of droplets and bubbles in microfluidic flow-focusing geometries. High viscosity and low interfacial tension of molten polymers makes it difficult to break a continuous fluid stream into drops. Furthermore, the eventual requirements that the polymers can only flow when heated far above room temperature require a new approach to fluid handling.

This thesis describes the development of a platform for molten polymer microfluidics based on a pressure-driven flow of polymer into micro-channels etched out of metal foils. This platform is developed for room temperature operation to test whether undiluted polymer melts can be emulsified in a controlled fashion in a microfluidic device. We report the results of a comparative study of microfluidic emulsification (i.e. drop or bubble formation) with different viscosities polymer liquids. At room temperature, depending on the properties of the polymer fluids and the flow rate, emulsification occurred in the dripping and jetting regions. We developed a simple circuit model to describe the observed dependence of the size of bubbles on the supplied pressure. The bubble shape, size, velocity, frequency were well investigated under various experimental conditions.

This study demonstrates the possibility of polymer drop formation in the room temperature device that can be used to further research using polymers need high temperature to be melted.

TABLE OF CONTENTS

LIST OF TABLES

LIST OF FIGURES

PREFACE

This thesis would not have been possible without the guidance and the help of several individuals who in one way or another contributed and extended their valuable assistance in the preparation and completion of this study.

First and foremost, Dr. Sachin Velankar, my advisor, under his guidance that I could complete this research works.

Dr. Shailesh Nagarkar, always had kind concern and consideration regarding my academic requirements. He has been my inspiration and my good friend.

Alex Boardman, my best Lab mate, for his unselfish and unfailing support.

Justin Lowen, the undergraduate student, who assists me to finish the experiment data. I really appreciate his hardly work and advise.

Mechanical Engineering students, who help us to design the high temperature microfluidic device, thank their assistances.

My friends in the Chemical Engineering Department, who always give my some new ideas and moral support, I really appreciate it. And my friends in Pittsburgh and Taiwan, who always help me to deal with any problems, thank you for your patience.

Last but not the least, my lovely family who support my tuition without any doubts and encourage me all the time when I face any difficulties.

Shu-Che Peng

1.0 INTRODUCTION

Microfluidics is a branch of research that studies the design, fabrication, and operation of systems of microscopic channels that conduct fluids. Microfluidics usually refers the devices and methods that control and deal with the fluid flow on a micron scale [1]. It is a technology that seeks to control and manipulate small amounts (10^{-9} to 10^{-18} liters) of fluids, using channels with dimensions of tens to hundreds of micrometers [2]. There has been significant research on implementing such ideas with low-viscosity liquids, most frequently water, at room temperature. One branch of microfluidics concerns two-phase flows of liquids in microfluidic channels with the goal of making particles of controlled structure. The overall goal of this research is to transplant these technologies to molten polymers.

There are two challenges in the research. These are (1) high viscosity and low interfacial tension of molten polymers makes it difficult to break a continuous fluid stream into drops (2) high viscosity and high temperature requires completely new methods of fluid-handling. The goal of this project is a room temperature study using high viscosity polymers that will conduct the fundamental studies with high viscosity polymers that are liquid at room temperature, and also develop a platform suitable for handling such fluids. If

successful, this will pave the way for further research using polymers that are solid at room temperature

Chapter 2 is the review of literature on two phase flow in microfluidic devices, and in particular on devices aimed at generating drops. Chapter 3 is about materials, methods, and device development. The result and discussion of developing the methodology using gas/polymer to form bubbles, and two immiscible polymers is Chapter 5. Chapter 6 is the conclusions and suggestions for future work.

2.0 LITERATURE REVIEW

2.1 BACKGROUND

The first research in microfluidics developed in 1975 by S.C. Terry in the Stanford University [3]. However much of the development of microfluidics can be traced to a 1999 paper by the Whitesides group [4] on how flows in micro-channels can be controlled and used to pattern the channel itself Beyond the scientific development, the key idea in this paper was soft lithography to fabricate microfluidic devices inexpensively using silicone rubber. Shortly afterwards, two papers by the Quake group [5] and the Nakajima group [6], showed how two phase flow of oil and water in microfluidic devices could be used to generate drops of a precisely controlled and tunable size. Notably Nakajima also showed that if the drops were made of oil whose temperature was above room temperature, upon cooling the drops could be frozen to form solid particles. Since these articles, there has been tremendous amount of research on generating drops in micro-channels, using them as micro-reactors, as sample "carriers" for sensor applications, and as precursors for the formation of particles of controlled shape, size, and structure. This last application of particle fabrication is the main topic of interest of this thesis.

2.2 APPLICATIONS OF 2-PHASE IN POLYMER PARTICLES

The types of particles fabricated in microfluidic devices have drawn attention in different areas. The microfluidics device with its small size takes the advantages of low cost of fabrication, and high precision. Recently, such complex polymer particles have been considered in biological and analytical applications.

In biology, these polymer particles could be used to replace the standard enzyme-linked immunosorbent assay (ELISA) procedure [7]. These applications are still developing, and at this stage the ability to fabricate complex microstructures is ahead of their applications.

Enzyme-linked immunosorbent assay (ELISA) is a biochemical technique used broadly in immunology detection biosensor field. [8] It's a powerful tool can easily measure the antigen in the sample in a very easy way. The current methods of using ELISA technique are based on antibody-coated micro-titer plate format and require high sample consumption and time-consuming washing steps for detection. Recently, an interesting alternative way is using microfluidic technique to make micron polymer particles replacing the micro-titer plates [9]. The critical element in the approach is to use optically distinguishable polymer micro-particles, each of which is functionalized with an antibody against a protein of interest. Moreover, the multiple protein measurements can be made in a single sample at once. Due to the micro size of particles, it requires less sample consumption and rapidly detection than before. It can be more sensitive than the standard sandwich ELISA [7].

Kumacheva *et al.* [10] demonstrated a technique of fabricating Janus particles and three-phase particles using microfluidics. These particles can be synthesized by the UV light source. The potential application of Janus particles can be combination of two different or multifunctional properties materials into a single particle. Particles with oppositely charged hemispheres created an electric field can be remotely monitored. Its potential applications in the production of color electronic paper would be realized in the future.

Polymer particles find important applications in medical diagnostics, and drug delivery. Biodegradable polymers, such as poly (lactic-co-glycolic acid) (PLGA), for example, have been widely used for drug delivery to achieve such controlled drug release. [2-4]. Anderson et al [11] demonstrated the technique of polymer micro-particle fabrication by using PLGA/drug and Polyvinyl alcohol (PVA) in the microfluidic device. With the higher yields by the microfluidic method, particles prepared using the microfluidic approach has a significant advantage than the conventional fabrication, especially for expensive drugs.

2.3 PARTICLES IN MICROFLUIDIC DEVICES

2.3.1 Methods to solidify polymer particles

As mentioned above, many ways have been developed to generate liquid drops in a controlled fashion in microfluidic devices. To solidify the liquid drops into solid particles,

various mechanisms can be used. These are classified as 1) heat-based, 2) light-based, and 3) chemical-reaction-based methods. [12] In heat-based methods, high melting point oils have been be melted in high temperature, drops formed, and cooled down into solids at lower temperature. For example, Nakajima et al emulsified hydrogenated edible oils at high temperature, and subsequently the emulsion was cooled and solidified give citation. Alternately or a drop made of monomeric oil can be thermally polymerized into solid particles [6]. Kumacheva *et al.* [13] synthesized droplets using various oligomers, and then polymerized them thermally on the microfluidic device itself. If the channel size was larger than the drop size, the drops were spherical; otherwise they were confined by the channel during polymerization and hence non-spherical particles. In light-based methods, ultraviolet light is used to convert monomer drops them into solid particles by photo polymerization. Kumacheva *et al.* [10] demonstrated that using soft lithography to shape Janus particles from immiscible monomers by using UV light in the downstream. There are many other groups who have used UV polymerization in microfluidic devices [14, 15]. Doyle et al [16] patterned the flat drops before UV-curing them. Chemical reaction based methods are different since there are no other external technique, such as UV light or heating devices.
In these methods, a specific chemical is added separately for the polymerization. As gel materials, calcium alginate is the most commonly employed system for the gel formation [17]. The polymer droplet could be solidified by this chemical in specific time and certain region in the microfluidic channel [17].

Others use the UV-polymerization of single phase flow to make particles using a photo-mask. Chung et el [18] introduced the technique called “railed microfluidics”, an agile method to assemble microstructures inside fluidic channels. The Doyle group [19]

demonstrated a stop flow lithography method that polymerizes a fluid through projection lithography within a microfluidic device.

Finally, it is also possible to start not with drops, but with particles that can be assembled on a device in a specific fashion, and then joining these assemblies permanently. Solomon et al [20] report the approaches of assembling colloidal particles into assemblies and then sintering them in microfluidic devices.

The limitation of these methods is the materials that can be processed: light-based approaches rely on monomers that can be UV-cross-linked rapidly [10]. There are only few photo sensitive polymers and some hydrogels that can be solidified rapidly by using UV light. For chemical reaction based methods, they are require specific chemical functionality that can solidify the particles rapidly [17]. In this study, we are seeking to apply cooling based methods to solidify polymer and could be applied to most of polymers. Most materials either are liquid at room temperature or have very high melting temperatures. The goal of your project is to overcome these material limitations.

2.4 THREE MAJOR TYPES OF DROPLET GENERATION SYSTEM

2.4.1 T-Junction Based Droplet Formation

The earliest paper on droplet-formation in microfluidic devices [5] developed a T-junction shaped channel for generating drops. The channel geometry is shown in Figure 1 below. The dispersed phase flow is supplied from the lower branch and uniform-sized drops are

formed in the junction by due to interfacial tension driven breakup. Numerous later researchers have used this method [21-24]. Garstecki *et al.* [24] developed a theoretical model to describe the mechanism by which droplets and bubbles are formed in T-junction microfluidic device. Guillot and Colin [25] then developed a semi-empirical model to describe the transition from droplets forming to stable parallel streams at a T-junction. At sufficiently high flow rates, the drop formation does not occur; instead parallel "co-flow" flow occurs.

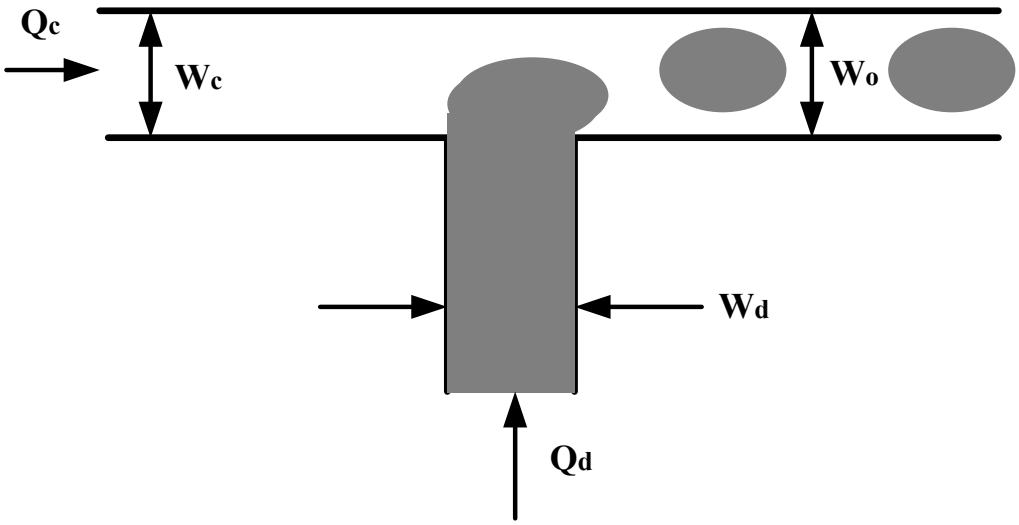

Figure 1 T-junction geometry to form drops

2.4.2 Flow-Focusing Device Based Droplet Formation

Another common geometry used for drop generation is the flow-focusing geometry in a microfluidic device shown in Figure 2 below developed by the Stone group [26]. The

dispersed phase flow is supplied through the middle channel, and two continuous flows come from two outer channels. These two liquid phases are forced through to a small constriction that is located downstream of the three channels. Numerous studies have used this approach [27-30]. In our study, we choose this geometry as our device geometry since the drop-forming fluid does not contact the side walls of the channel and hence wettability problems can be avoided. Utada *et al* [31] had a strong correlation that estimate the relationship of drop size and the flow rate in the flow focusing geometry channel. Some researchers have used the same geometry without a constriction and this is sometimes called a cross-flow junction.

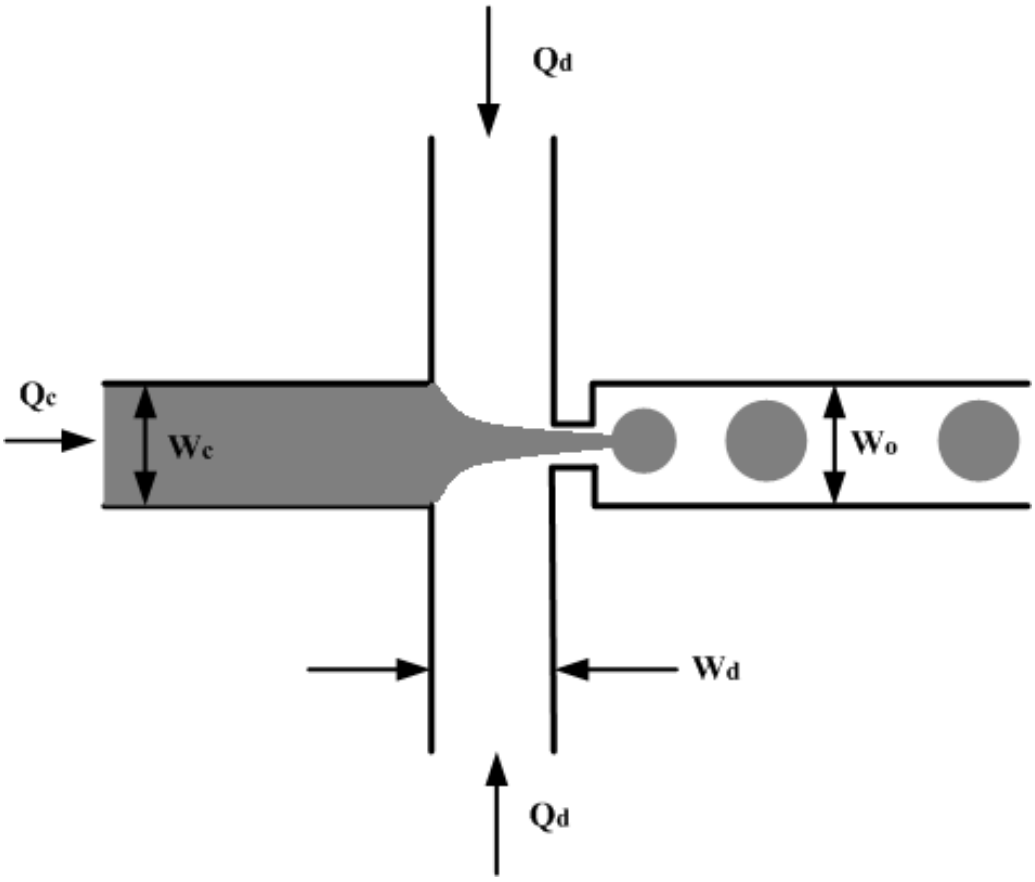

Figure 2 Geometries used in flow-focusing microfluidic devices.

2.4.3 Co-flow Based Droplet Formation Devices

Co-flow based geometry shown in the Figure 3 is when the two fluids flow parallel to each other and form drops [32-35]. This flow geometry is similar to numerous traditional drop generating devices such as spray nozzles or emulsifiers. Sometimes there is a collector tube of diameter intermediate between the inner and the outer tubes; this collector is placed with its inlet a small distance away from the inner tube. Umbanhowar *et al.* [36] described this experimental technique for the production of highly mono-disperse emulsions.

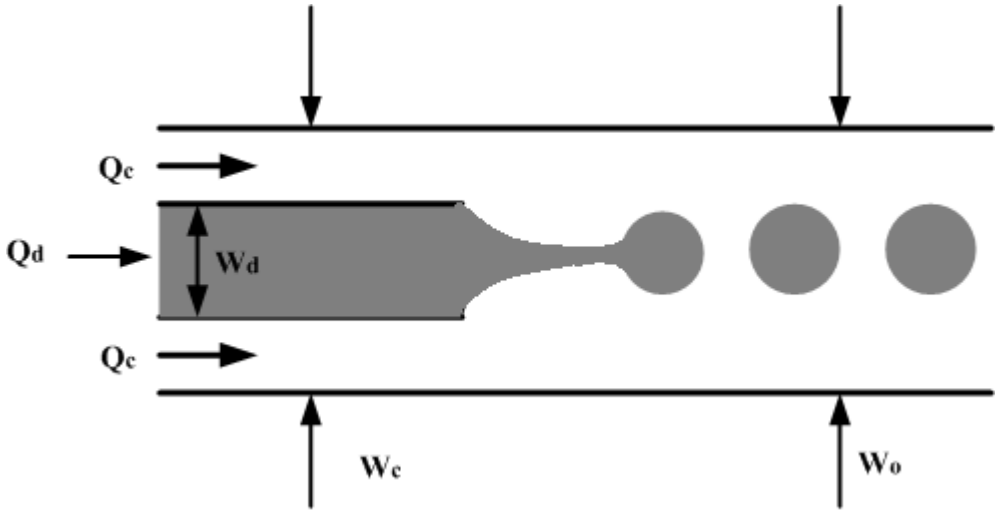

Figure 3 Geometries used in co-flow microfluidic devices.

2.5 CAPILLARY NUMBER AND CHALLENGE FOR MOLTEN POLYMER MICROFLUIDICS

Two-phase flows are determined by the balance of inertial force, viscous drag forces, interfacial tension forces, and buoyancy forces. The Reynolds number (Re) is a dimensionless number that gives the ratio of inertial forces to viscous forces and quantifies the relative importance of these two forces under given flow conditions:

$$\mathrm{Re} = \frac{\rho v D}{\mu} \tag{1}$$

where ρ is the fluid density (kg/m^3), v is the velocity (m/s), D specifies a characteristic length scale (m), and μ is the viscosity of the fluid (Pa.s). The Bond number (Bo) determines the relation between gravitational forces and surface tension forces:

$$\mathrm{Bo} = \frac{\Delta\rho g D^2}{\gamma} \tag{2}$$

where $\Delta\rho$ is the fluid density difference (kg/m^3), γ is the surface tension between the two fluids (N/m), and g is the gravitational acceleration (m/s^2).

In microfluidic flows, the Reynolds and Bond numbers are very small and hence it is safe to ignore gravitational forces and inertial forces. The two dominant forces are surface tension forces and viscous drag forces. The Capillary number (*Ca*) is defined to the ratio of viscous drag forces and surface tension forces:

$$Ca = \frac{F_{viscous}}{F_{surface}} = \frac{\mu v}{\gamma} \tag{3}$$

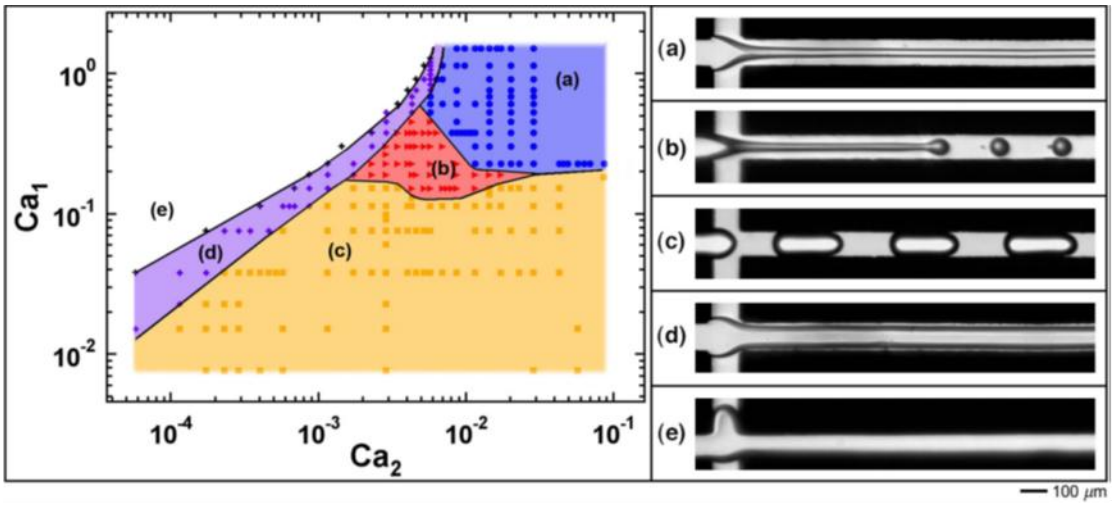

Figure 4 Flow map based on the capillary number with various flow regimes. a): threading b): jetting c): dripping d): tubing e): viscous displacement. Fluid 1 here is the dispersed phase fluid, and fluid 2 is the continuous phase fluid. Reprinted with permission from the authors [37].

All theories and experiments of drop formation and behavior in micro-channels involve *Ca* as the primary dimensionless parameter. For example, Cubaud *et al.* [37] examined two-phase flow in a cross-flow junction. They represented their results in the form of a flow map that depends on two capillary numbers, one for the inner fluid, and one for the outer fluid. This map (Figure 4) distinguishes the following flow regions: a): threading b): jetting c): dripping d): tubing e): viscous displacement. In our research, we are interested the dripping and jetting phenomena these are the ones that can give rise to drop formation. From this map, it is clear that the droplets or bubbles are formed when *Ca* is less than about 0.1. The viscosity of polymers is about 5 orders of magnitude larger than in oil/water systems, and the interfacial tension is an order of magnitude lower. Thus, at any reasonable flow rate, it means the *Ca* is extremely high when a molten polymer is to be used. Reducing the *Ca* sufficiently low to allow drop formation would require flow rates

that are six orders of magnitude lower than in oil-water systems. This is a fundamental challenge in implementing drop-generation systems with molten polymers.

2.6 CHALLENGES: HIGH VISCOSITY, HIGH TEMPERATURE, AND LOW TEMPERATURE; CAPILLARY NUMBER

As mentioned in the introduction, the goal of this project is to use microfluidic devices to make drops out of molten polymers and then cool them to form solid particles. Here we will list the chief challenges.

2.6.1 Fundamental challenge

The capillary number issue mentioned above is the chief fundamental challenge of this research; it arises from factors (high viscosity and low interfacial tension) which cannot be circumvented. The high viscosity of polymers and the lower interfacial tension increase the difficulties to make droplets in the micro channels.

2.6.2 Practical challenges

The first most obvious challenge is that some portions the device must be designed to operate at high temperature, but furthermore, prior to exit from the device, the molten drops must also be allowed to cool down to solidify them. Secondly, maintaining visibility in the junction area -along with the high temperature requirement- greatly constrains selection of

window materials. Lastly, the very high viscosity of molten plastics means that pinching off the continuous flow to form drops is more difficult; instead, there is a tendency to form a co-flow of continuous streams. PDMS devices, which are extremely common in research on microfluidics can no longer be used since the microfluidic device must be operated at high temperature and pressure. Finally, in past research on oil/water systems, syringe pumps were generally used to control the fluid flow rate. With the high temperature system, the syringe pumps could not be easily used because of the temperature requirement to melt the solid polymer. While the syringe itself could be maintained hot, it is much more difficult to maintain in a high temperature in the tubing that connects the syringe pumps to the devices. Furthermore, the low flow rates would imply a long residence time in the tubing, with thermal degradation due to the high temperature. Therefore the polymers need to be stored in small quantities in molten form on the device itself.

2.7 TECHNICAL APPROACH

Moon *et al.* [38] demonstrated that metal shims (i.e. foils) could be used to construct channels for microfluidic flow of molten polymers. The shims were machined with micro-channels and then sandwiched between hard surfaces. Since visibility is needed they constructed the windows out of sapphire. The polymer was stored on the device, and in fact was a single pellet of plastic. The chamber of the molten polymer was exposed to controlled pressure to drive flow. Thus, syringe pumps and external tubing was not used:

the pressure control system was be used to drive the flow. By adjusting the pressure value, the microfluidic flow rate could be varied.

We seek to build upon these ideas further to build microfluidic devices that can generate drops.

2.8 PREVIEW OF THIS RESEARCH

In summary we aim to develop a new approach for implementing microfluidic devices that can generate drops from molten polymers. This requires solving many practical problems mentioned above as well as one fundamental one of whether drop breakup will occur even when bulk viscosity is so high. This thesis seeks split the challenges into two parts: first developing the shims and pressure control system, and testing whether drops can be formed at reasonable flow rates, and second, how to implement his device at high temperature. This thesis addresses first two challenges.

In this study, we are focusing on using pressure driven control system to drive the polymer flows at room temperature. Our target is to study the high viscosity microfluidic polymer flow at room temperature to find out whether drop formation is feasible. The research result could be used later in the high temperature microfluidic study.

3.0 MATERIALS AND METHODS

As mentioned in the previous chapter, the goal of this thesis is to test out the basic ideas of fluid handling and to address the fundamental challenges of inducing droplet breakup with molten polymers, but to do so at room temperature. The issue of the high temperature device is left for the future.

3.1 MICROFLUIDIC PLATFORM DESIGN

The experiment system in this study is shown in Figure 5. We will discuss three portions separately: the microfluidic device, the driving force for flow, and the data acquisition. The microfluidic device is shown in Figure 6. The outer platform (Figure 7, Figure 8) of the microfluidic device was fabricated from acrylic (polymethyl methacrylate, PMMA), with two reservoirs for holding two different polymers. For the research in Chapter 5, one of the reservoirs was filled with the continuous polymer liquid phase, whereas the other was empty, allowing nitrogen gas to be fed through.

The geometry of the channels here is flow-focusing with the widths of the main channels being 381μm, and the constriction (127μm) in the intersection as will be shown later in Figure 14.

Early experiments used a single layer of metal foil to fabricate the channels. These devices suffered from severe wettability problems related to the fact that the dispersed phase made contact with the top and bottom surfaces of the flow channels. In oil/water systems, it is common to use surfactants to control which phase wets the solid surfaces; however, effective surfactants are not available for controlling the wettability of molten polymers. Therefore it is crucial to prevent the dispersed phase fluid from contacting the walls of the channel. Accordingly the device was redesigned in three layers. The channel was constructed in three layers made of three different metal shims to avoid wetting problems, i.e. to avoid the dispersed phase from touching the top and bottom walls. The thickness of bottom and top shims were 125μm (Figure 9), and the middle shim was 250μm (Figure 10). Dispersed phase is supplied through a channel in the middle shim (Figure 11, Figure 12). When assembled, the device geometry (Figure 13) ensures that the dispersed phase does not touch the top or bottom walls as it is introduced.

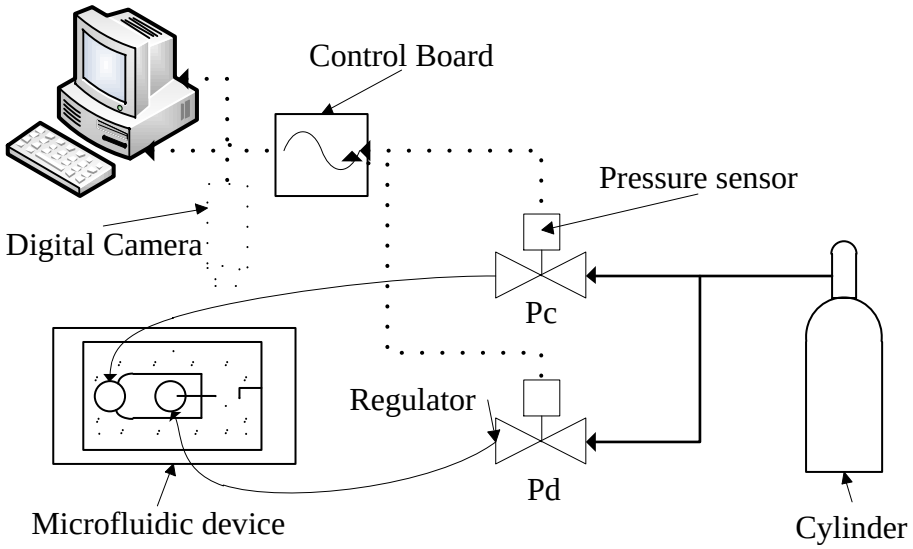

Figure 5 The experimental setup. Dotted lines here are the electrical wires, and the solid ones are the nitrogen gas lines

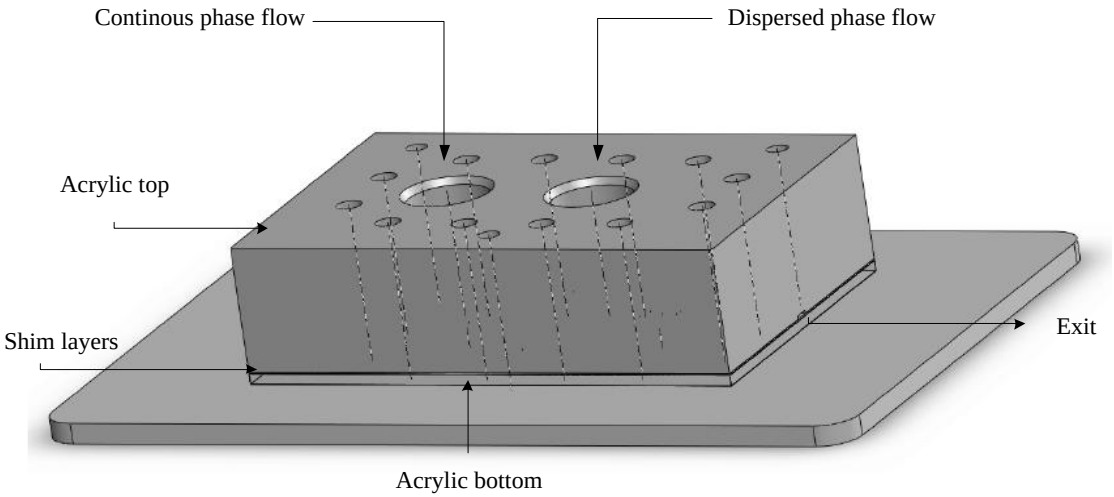

Figure 6 Microfluidic setup for the two-phase flow in a flow-focusing geometry. The microfluidic device is mounted on an inverted microscope.

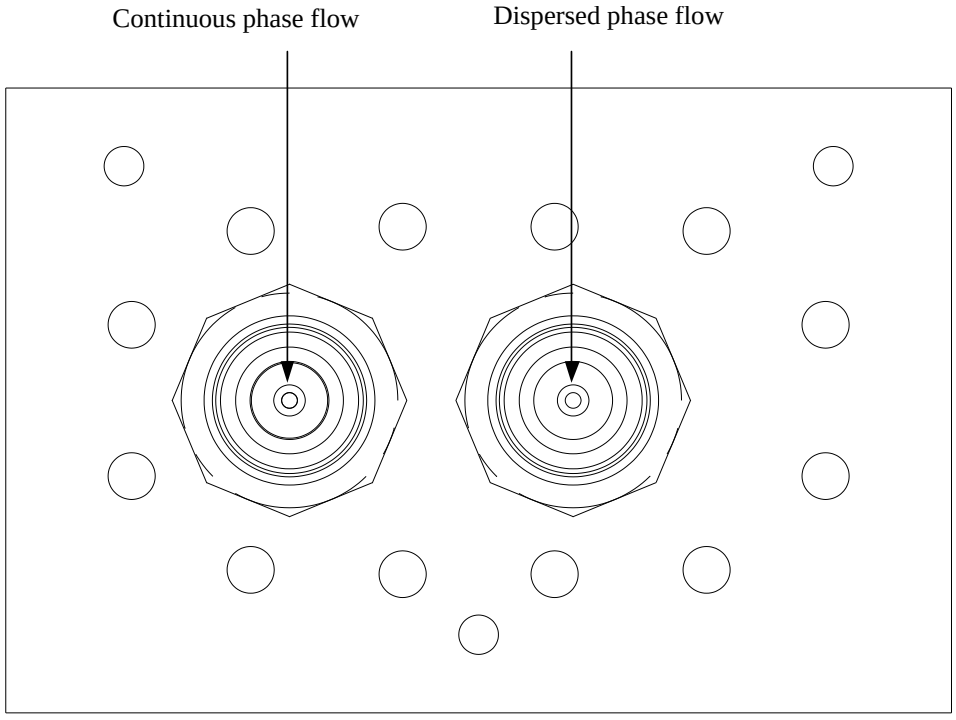

Figure 7 The acrylic platform as viewed from the top.

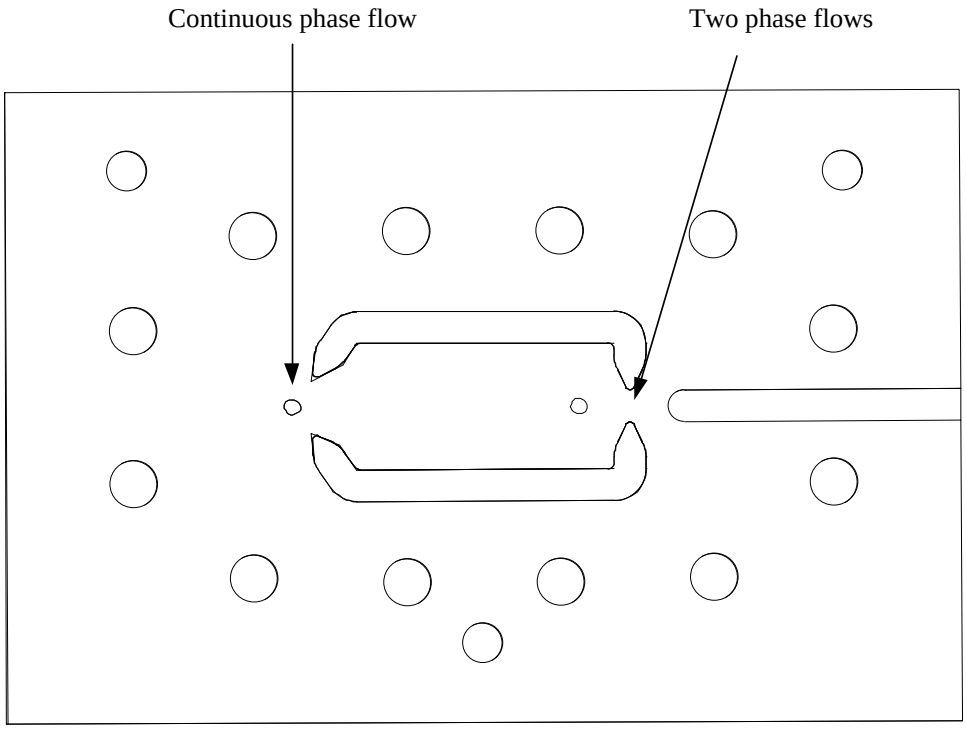

Figure 8 The acrylic platform viewed from the bottom.

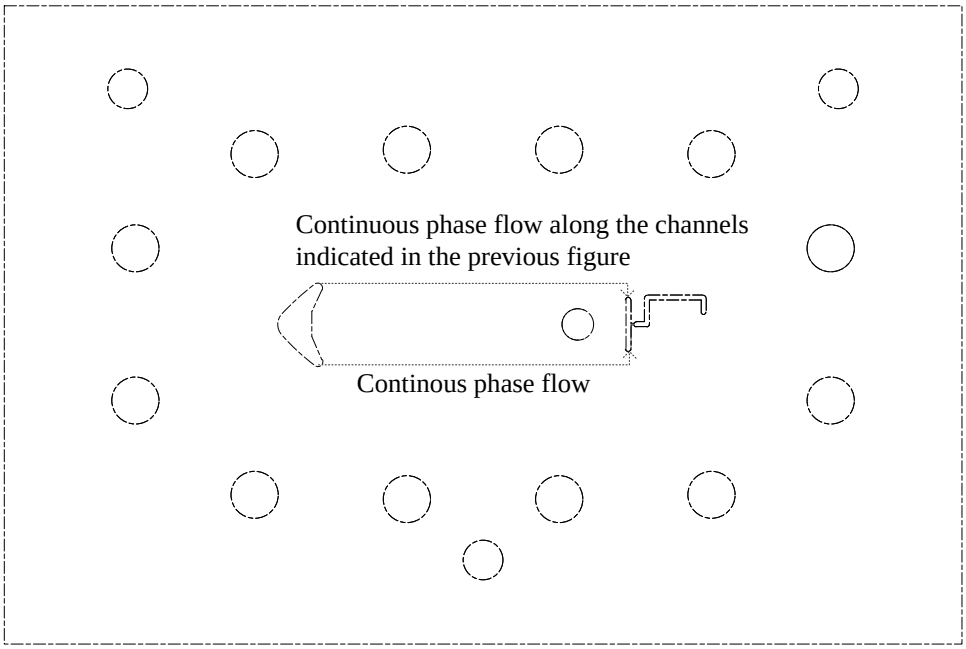

Figure 9 The bottom views of the acrylic platform.

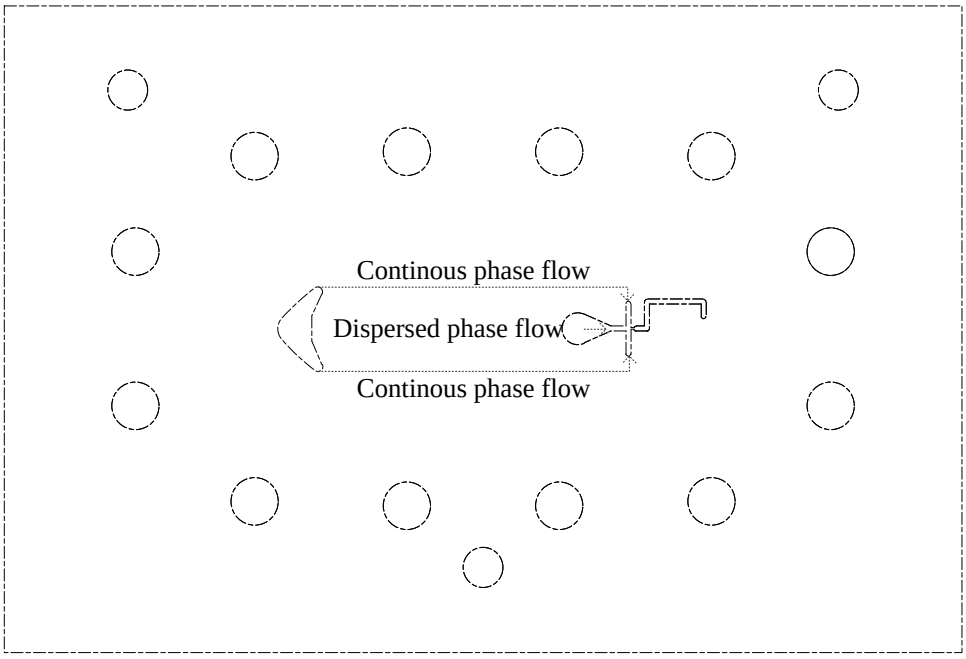

Figure 10 The scheme of the middle shim.

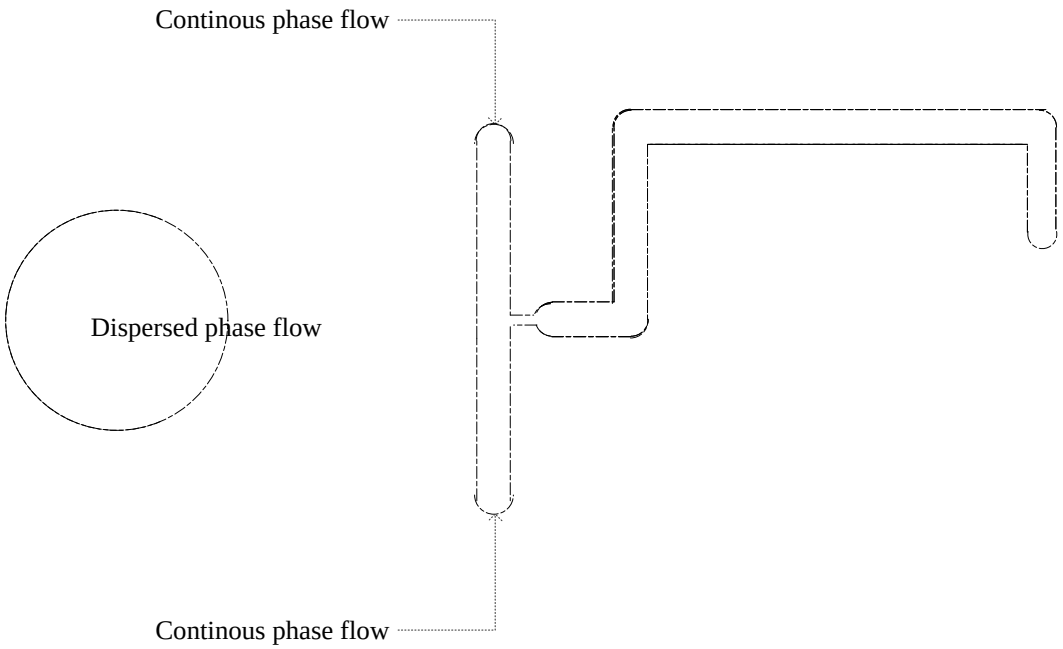

Figure 11 Magnified view of the junction region in the top and bottom shim layers.

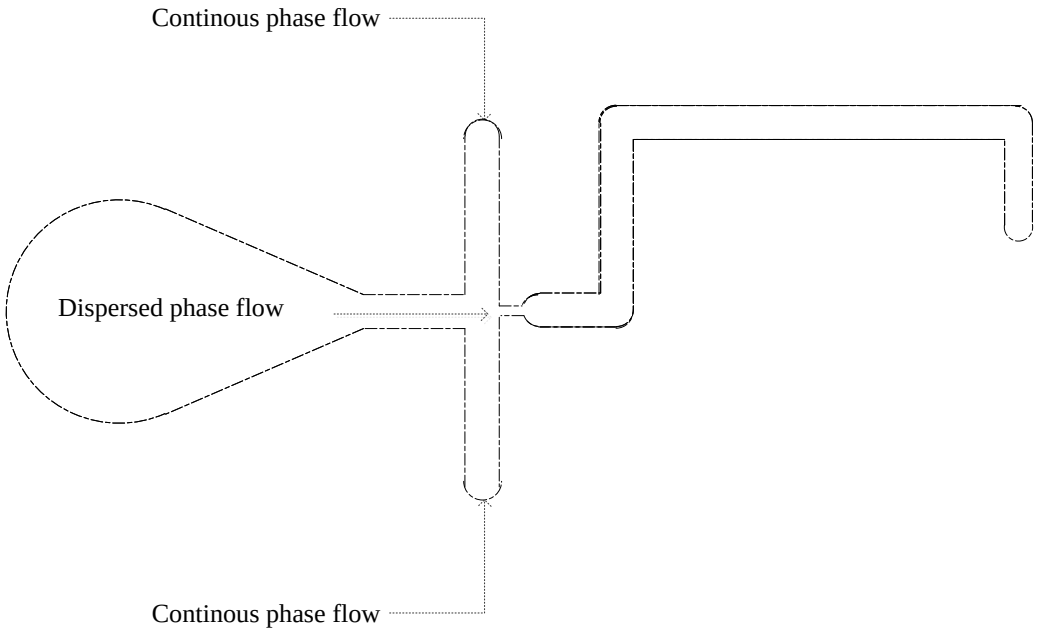

Figure 12 Magnified view of the junction region in the top and middle shim layers.

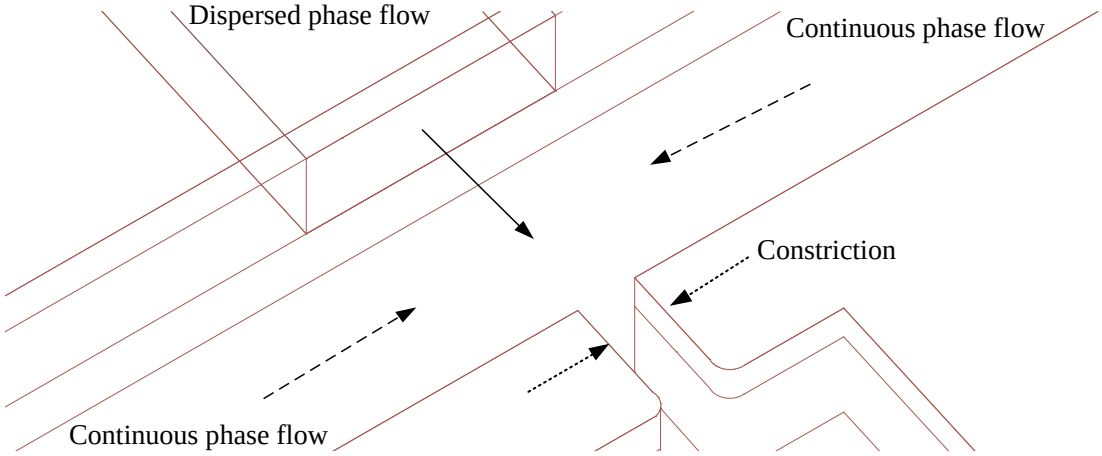

Figure 13 The scheme of the three metal shims stacked. The dispersed phase flow from the middle shims could avoid the wettability problem.

3.2 DRIVING THE FLOW: REGULATORS, THE CONNECTORS, SENSORS

The Nitrogen gas cylinder was connected to two regulators to supply air pressure. The pressure regulators, 78-4 (Melotieanon), were used to maintain the constant pressure required to push the polymers and the nitrogen gas streams into the channels. The regulators were connected to the microfluidic device with 1/8" tubes and 1/4" to 1/8" quick-disconnect fittings. Two 15 psi pressure sensors, 26PC15 (Honeywell), were used to determine the pressure being applied. In each experiment, the continuous phase pressure was fixed at a certain value, and the dispersed phase pressures was varied to examine the various flow conditions under which two phase flow can be realized.

3.3 DATA ACQUISITION: MICROSCOPE, CAMERA, AND THE IMAGE ACQUISITION.

The voltage values output by the pressure sensors were read by a controller board, 6014 (NI instruments), connected to a computer. The pressure values and experiment time were recorded by software (Lab-view). Images of bubbles and droplets were captured with a 4X microscopic objective and recorded by a microscope digital camera, EO-1312M (Edmund Optics, Germany. The acquisition rate was 13 frames per second with a 1280X1024 resolution.

3.4 MATERIALS

Nitrogen gas and polyisoprene (PI) was used as the dispersed phase and three polydimethylsiloxane (PDMS) liquids with various viscosities were used as the continuous phase. Table 1 shows some of the relevant properties of the fluids used. The two pressure regulators were controlled from 4-12 psi to realize different flow conditions. All experiments were conducted at room temperature.

Table 1 Properties of the fluids used at room temperature [1]

fluid	$\rho(kg \cdot m^{-3})$	$\mu(Pa \cdot s)$	Supplier
PDMS 30K	965	30	Rhodia
PDMS 100K	965	100	Rhodia
PDMS 500K	965	500	Rhodia
PI (LIR30)	910	131	Kuraray America
PEO400	1128	$108*10^{-3}$	Aldrich
Water	1000	$1*10^{-3}$	N/A
Nitrogen gas	1.251	$17.81*10^{-6}$	Penn Oxygen

[1] PDMS viscosities are measured by the manufacturer. PI viscosity was measured in house on a rheometer.

4.0 RESULTS AND DISCUSSION

Before undertaking two phase flow experiments with immiscible polymeric fluids, several experiments were conducted with air as the dispersed phase and a room-temperature molten polymer (PDMS) as the continuous phase. One significant advantage of this is that wall-wettability is not an issue: the walls are completely wetted by PDMS. The goals of the experiments are to verify operation of the system in room temperature, to test for any leakages, and most importantly to find out conditions under which bubbles are formed.

4.1 GAS-LIQUID SYSTEM

4.1.1 The geometry of the Flow-focusing channel

Figure 14 illustrates the geometry of a flow-focusing junction. The PDMS continuous fluid flows from the side-channels and pinches off the air bubbles from the air stream supplied in the middle channel. The channels have rectangular cross sections with a narrow constriction. The channels width *w* here are 381μm, and the constriction *a* is 127μm.

The experiments consisted of forcing PDMS and air through the device at various combinations of pressure; recording video of the flow at the junction and downstream of the junction. The gas and PDMS pressure values range from 5-12 psi

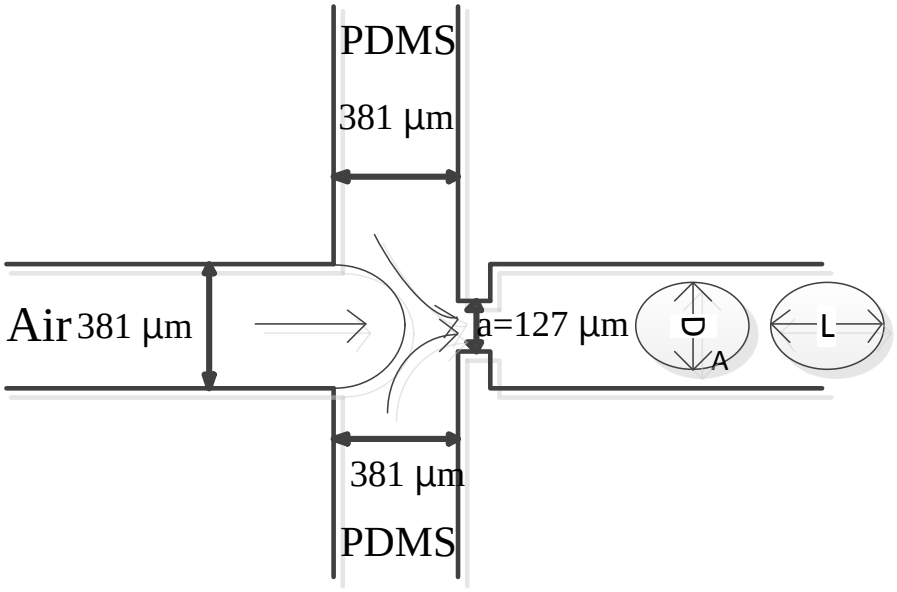

Figure 14 Geometry of the cross flow junction along with dimensions. Bubbles are formed in the junction and their geometry is specified by their length L and width D.

4.1.2 Bubble formation

In each experiment, the P_c value was kept fixed and P_d was increased gradually to identify the range of P_d values in which bubble formation was evident. This process was repeated at successively higher values of P_c. The whole process of bubble formation in the flow-focusing geometries can be described as follows: PDMS fluid and air form an interface at the intersection of the channel. As the air pressure P_d is increased, at a certain pressure, bubbles began to form at

a regular frequency. The time sequence of the whole bubble formation process is shown in Figure 15. When the pressure P_d was increased further, at some higher value, instead of steady formation of bubbles, the flow became irregular without regular pinch off of discrete bubbles as shown in Figure 16.

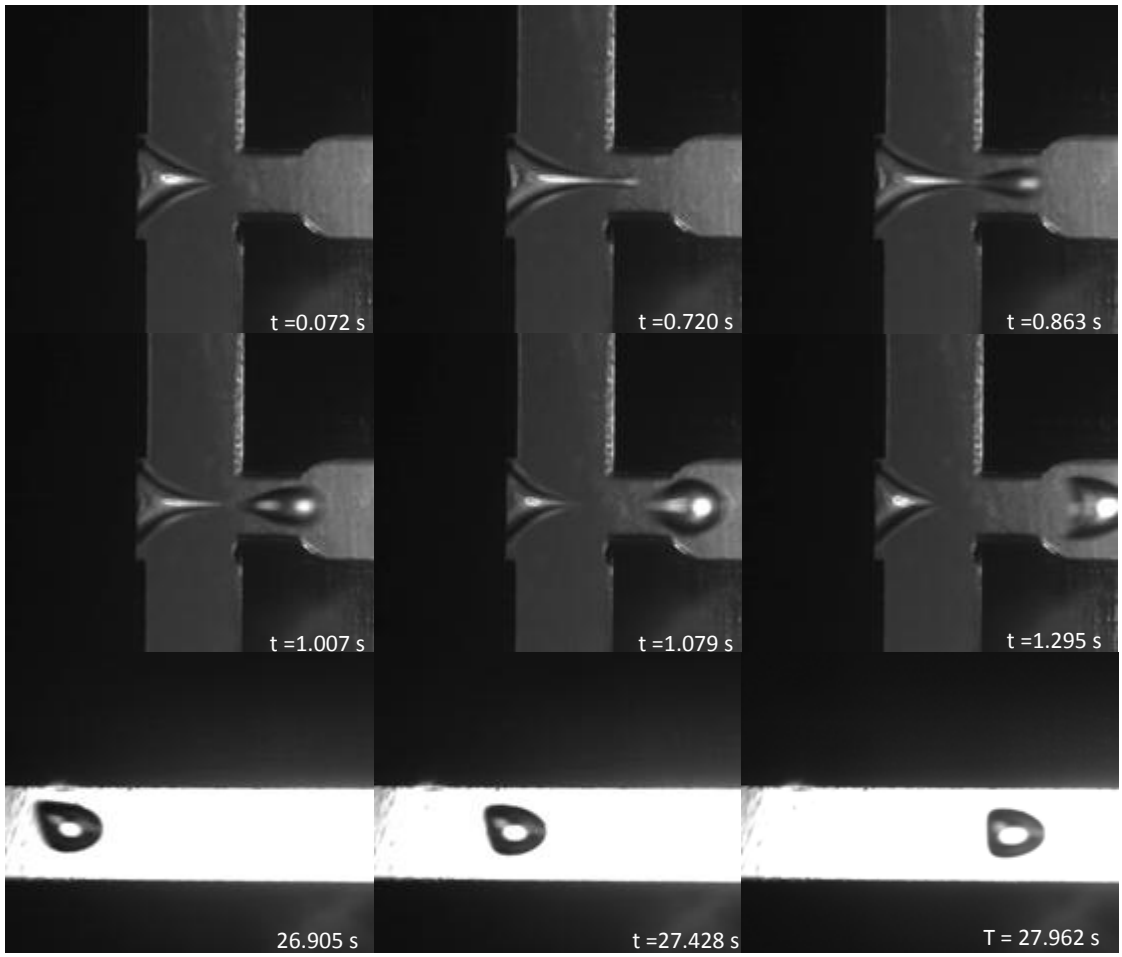

Figure 15 The bubble formation in the flow-focusing junction. The continuous phase liquid is PDMS 30K. The continuous phase pressure is $P_c = 5$ psi and the dispersed phase is $P_d = 3.18$ psi. The upper six images show the time sequence of bubble formation in the junction. The lower three images show the bubble being convected downstream.

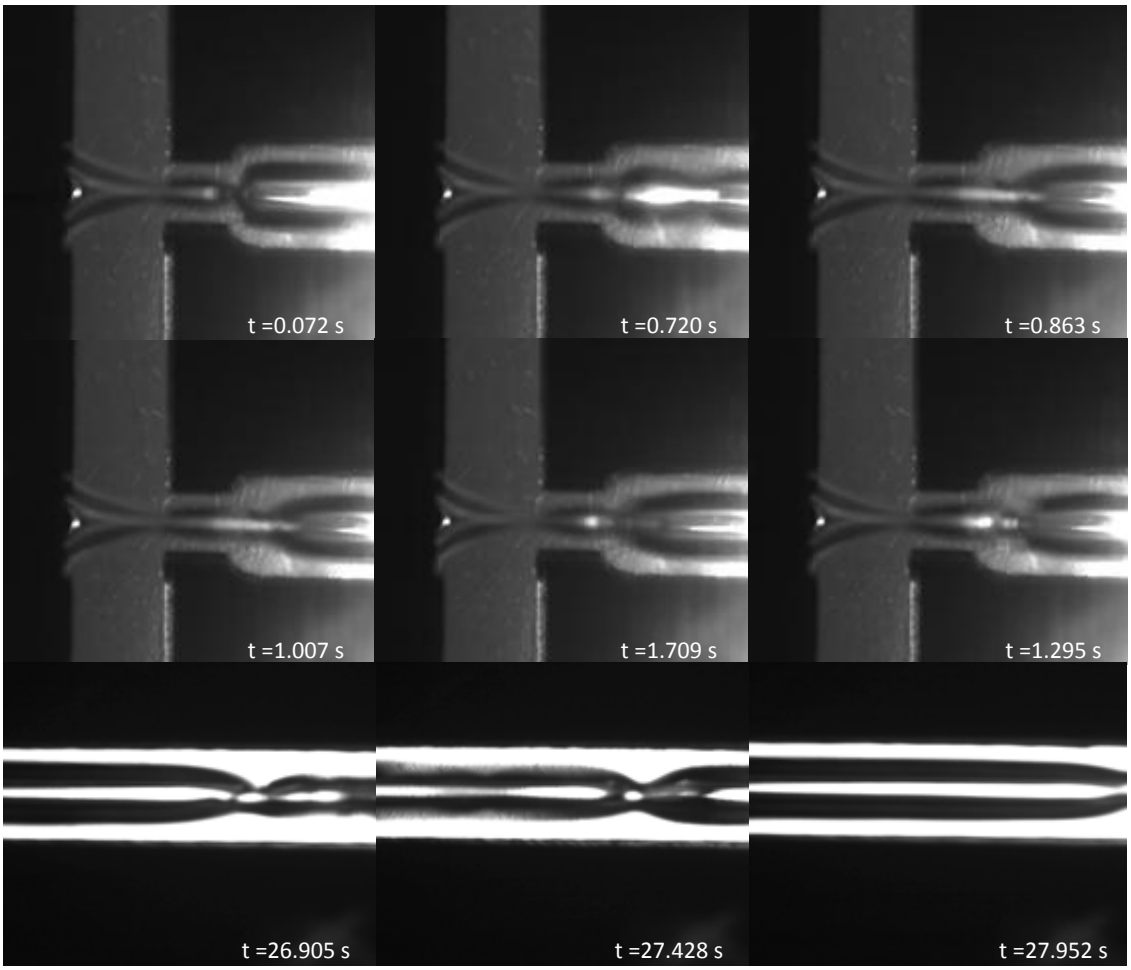

Figure 16 The Irregular "tubing" flow in the flow-focusing cross-section. The continuous phase liquid is PDMS 30K. The continuous phase pressure is P_c = 5 psi, and the dispersed phase is P_d = 3.18 psi.

In the range of P_d values in which bubble formation is evident, there is a large dependence of bubble size, frequency, and velocity on P_d. Each of these dependences is explored below. But before proceeding, it is important to establish a procedure whereby the size of the bubbles can be estimated in a consistent fashion.

Figure 18 shows a schematic diagram of the typical bubble shape in our experiments. Since the bubbles are not spherical, we need some systematic procedure to estimate the bubble volume consistently. Therefore we have developed the following procedure for doing so, assuming that the bubble is axisymmetric. The overall goal of the procedure is the find the volume of an equivalent cylinder whose cross-sectional area matches the cross-sectional area of the bubble. The width D of the bubble can be measured directly from the image. We first use the "find edges" function in ImageJ to find the boundary of the bubble. Then, the area of the bubble, A, in the frame can be determined by the "measure area" function in ImageJ. If this area is equated to the cross-sectional area DL of the equivalent cylinder, the effective length L can be obtained simply as A/D.

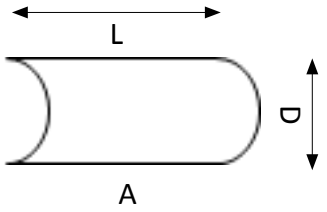

Figure 17 The diagram of the bubble illustration.

The volume of the equivalent cylindrical bubble V (Figure 17) is simply obtained as:

$$V = \pi\left(\frac{D}{2}\right)^2 L \tag{4}$$

In many cases, we are interested not in the volume, but in the diameter which can be calculated as:

$$d = 2 * \left(\frac{3}{4}\frac{V}{\pi}\right)^{-3} \tag{5}$$

To consider the possible errors, we illustrate three limiting types of the bubbles for discussions in Figure 18 and Figure 19 to calculate the error in estimating the bubble volume and diameter. The first type is the cylinder shape of the bubble. For sufficiently long cylinders, the above procedure will cause no error in estimating the volume when we apply above procedure. For short cylinders, error may be expected. In the limiting case of a short cylinder, we may spherical bubbles.

The volume of the sphere is:

$$\mathrm{V} = \frac{4}{3}\pi\left(\frac{D}{2}\right)^3 \tag{6}$$

The projected area is $P_i * D^{2/3}$. Thus the length L of the effective cylindrical bubble can be obtained as:

$$\mathrm{A} = \pi\left(\frac{D}{2}\right)^2 = D * L \tag{7}$$

$$\mathrm{L} = \pi * \frac{D}{4} \tag{8}$$

The axisymmetric shape volume for the cylinder shape:

$$\mathrm{V} = \frac{D}{4}\pi\left(\frac{D}{2}\right)^2 \tag{9}$$

Thus, the diameter error of spherical shape is about 8 %, which may be regarded as an acceptable level of error. Finally we consider the crescent shape of the bubble. We simply illustrate this shape with two spheres overlapped in the radius $\frac{D}{2}$ (Figure 18).

The volume of this moon-shape bubble:

$$\mathrm{V} = \frac{11}{12}\pi\left(\frac{D}{2}\right)^3 \tag{10}$$

The area of the moon-shape is now equated to the effective cylinder area DL:

$$A = \frac{4\pi - 3\sqrt{3}}{12}\left(\frac{D}{2}\right)^2 = D * L \tag{11}$$

$$L = \frac{2\pi + 3\sqrt{3}}{12} * \left(\frac{D}{2}\right) \tag{12}$$

The axisymmetric shape volume for the cylinder shape:

$$V = \frac{2\pi + 3\sqrt{3}}{12}\pi\left(\frac{D}{2}\right)^3 \tag{13}$$

Thus, the diameter d error of moon-shape is about 1.5 %, once again an acceptable level of error

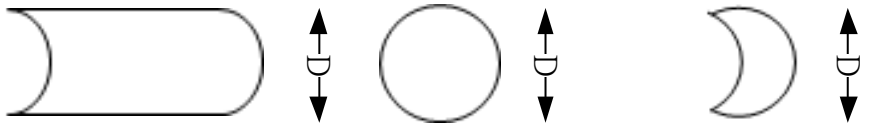

Figure 18 Three major types of the bubble shape.

Figure 19 A schematic illustration of the bubble formation.

In summary, we conclude that there is relatively little error in estimating the bubble diameter by the procedure developed here.

Figure 20 shows that while the bubble sizes do not change across a large range, there is a very large dependence of the bubble size on the dispersed phase pressure. Compared to flow rate controlled systems, a similar changes in bubble size requires orders of magnitude increase in

dispersed phase flow rate [39, 40]. In contrast, in the pressure-controlled situation discussed here, the same change in diameter is caused by only a few percent increases in P_d

The bubble velocity versus the dispersed pressure for various values of Pc is shown in Figure 21, and also found to change significantly as P_d increases. This trend is puzzling since in the current experiment, the P_c is kept constant, and P_d changes only a few percent, therefore, a large increase in total flow rate is not expected. Thus we had expected the bubble velocity to increase only slightly with P_d. In contrast, experimentally the bubble velocity is found to grow rapidly with dispersed phase pressure.

The results for the frequency of bubble formation are shown in Figure 22. Again, the frequencies increase sharply as the dispersed phase pressure grows. The frequencies increase almost linearly with P_d.

Finally, Figure 24 shows the flow map, i.e. the combinations of pressure within which bubbles can be generated. It is clear that there is a relatively narrow range of P_c and P_d values in which bubble formation occurs. This is in sharp contrast to flow rate-controlled systems in which bubbles (or drops) can be generated across a wide range of flow rate ratios.

One quantity of interest in these situations is the capillary number, *Ca*. For the PDMS/air interface, σ is known to be about $20\,\frac{\mathrm{mM}}{m}$. The Ca calculated accordingly is shown in Figure 25, and of course it follows the same trend as the velocity. Notably, the capillary numbers are far larger than noted in Figure 4 (the largest *Ca* value in Cubaud et al is $Ca = 10^{-1}$ [37].)

Reynolds's number (Re) here:

$$\mathrm{Re} = \frac{965\ \frac{kg}{m^3} * 1000 * 10^{-6}\frac{m}{s} * 4\frac{(381 * 500)}{2(381 + 500)} * 10^{-6}m}{30\frac{kg}{m.s}} \quad (14)$$

$$= 1.39 * 10^{-5}$$

Bond number (Bo) here:

$$\mathrm{Bo} = \frac{964\ \frac{kg}{m^3} * 9.8\frac{m}{s^2} * (250 * 10^{-6})^2 m}{19 * 10^{-3}\frac{kg}{s^2}} = 3.1 * 10^{-2} \quad (15)$$

Both Re and Bo are far less than 1 indicating that inertial and gravitational effects are weak: the flow is dominated by viscous and surface tension forces.

Based on the value of the capillary number, an extrapolation of Cubaud's results suggest that a flow in the dripping regime may be expected. And it looks like we could get drop or bubble formation at far higher capillary values than Cubaud. The reason is not clear but it is not because we used a gas as the dispersed phase (rather than a liquid). In fact, in the following chapter, we will demonstrate the similar results using water as our dispersed phase flow. The extreme viscosity ratio may be one of the reasons. Indeed, it must be noted that in Cubaud et al the velocity was known exactly since the flow rates were specified. In our case, the gas phase velocity is measured from video microscopy.

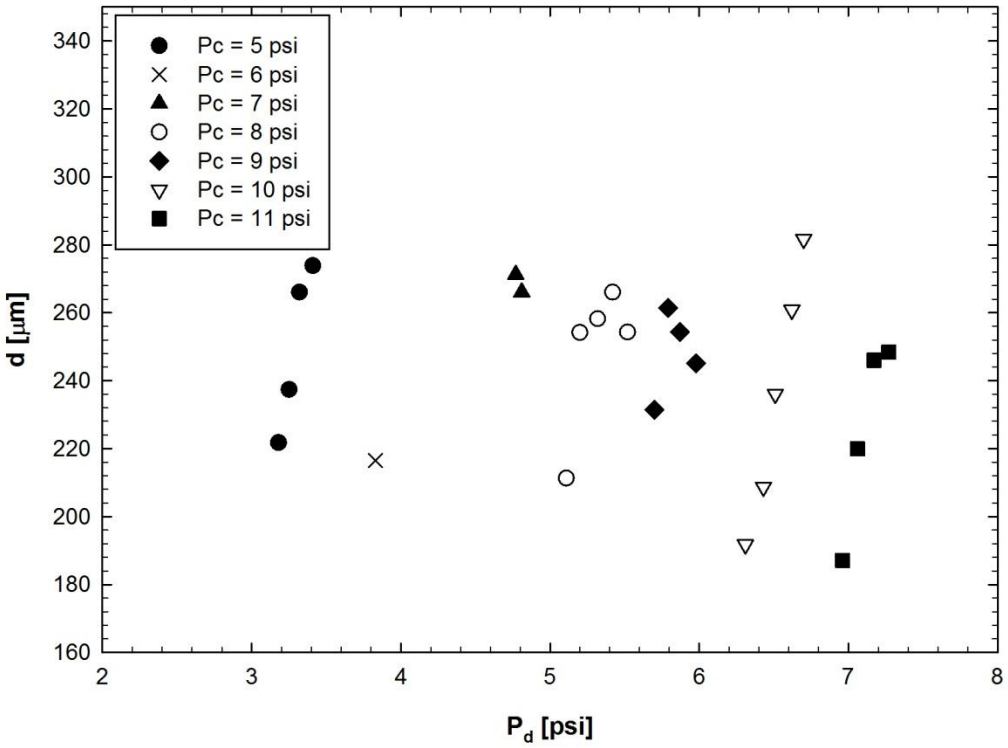

Figure 20 Highly dependence of size on P_d

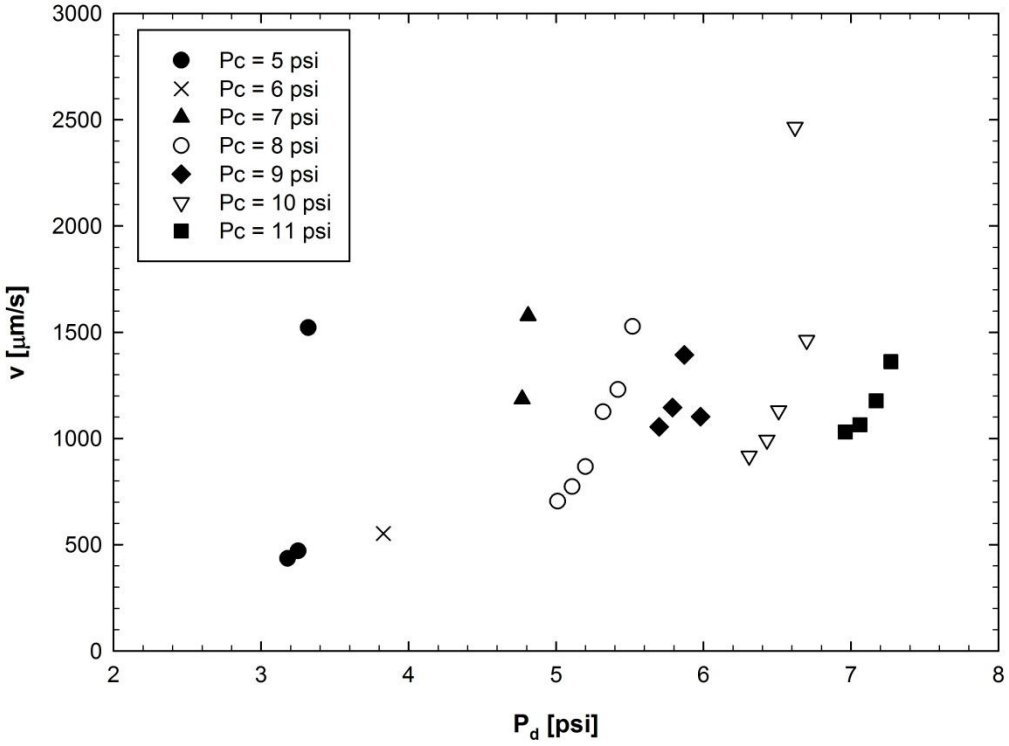

Figure 21 Dependence of bubble velocity P_d at various values of P_c.

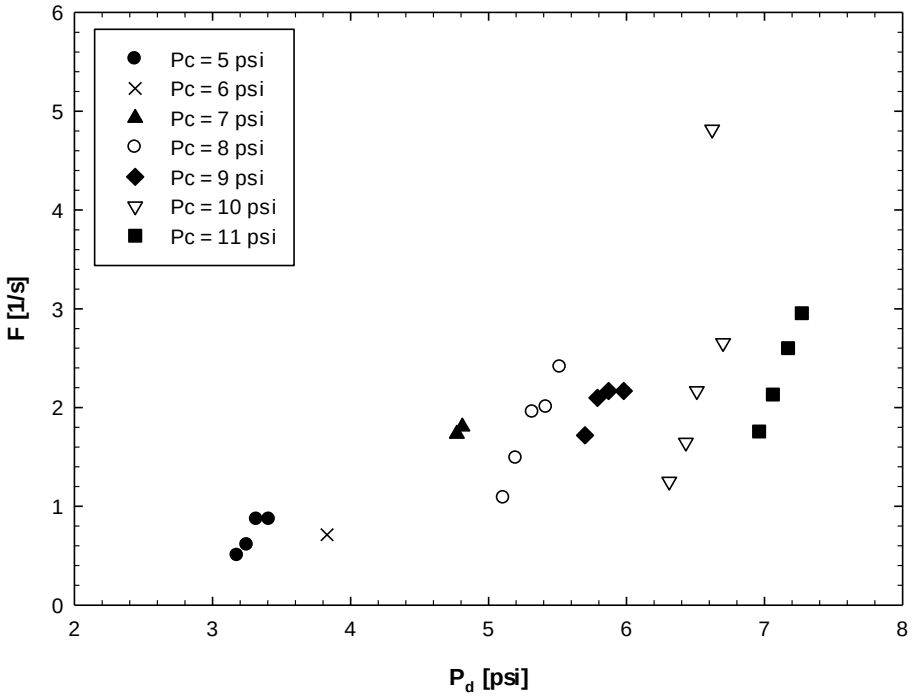

Figure 22 Frequency is almost 2 -3 times faster when narrowed P_d changes applied.

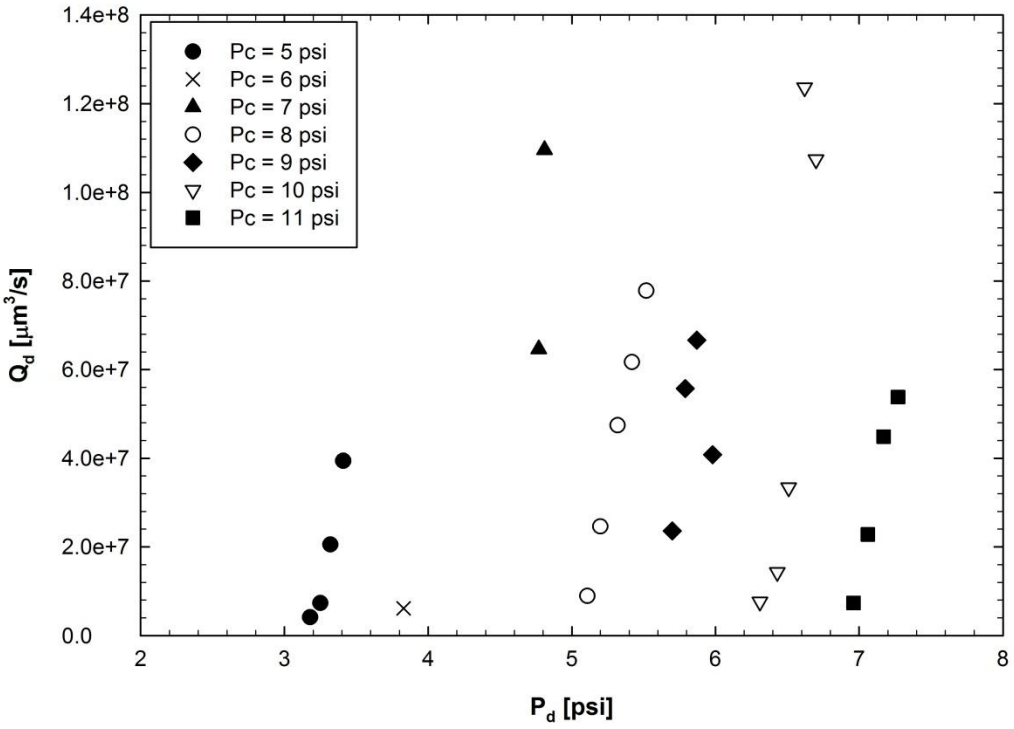

Figure 23 Dependence of the dispersed phase flow rate Q_d (= bubble volume x bubble frequency) on P_d at various values of P_c

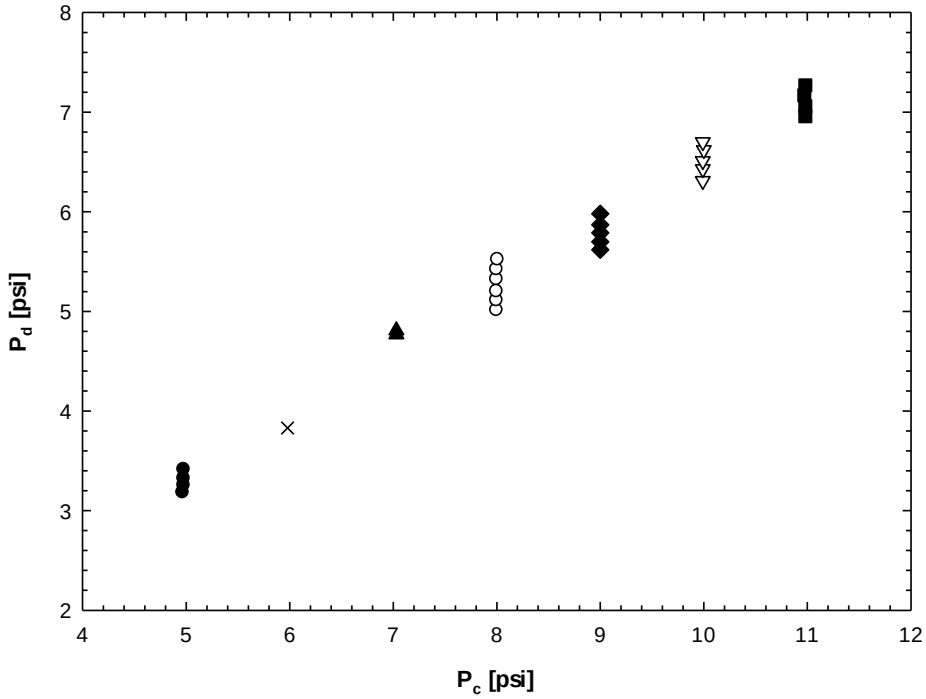

Figure 24 The combinations of continuous fluid pressure (P_c) and dispersed fluids pressure (P_d) at which bubbles can be generated.

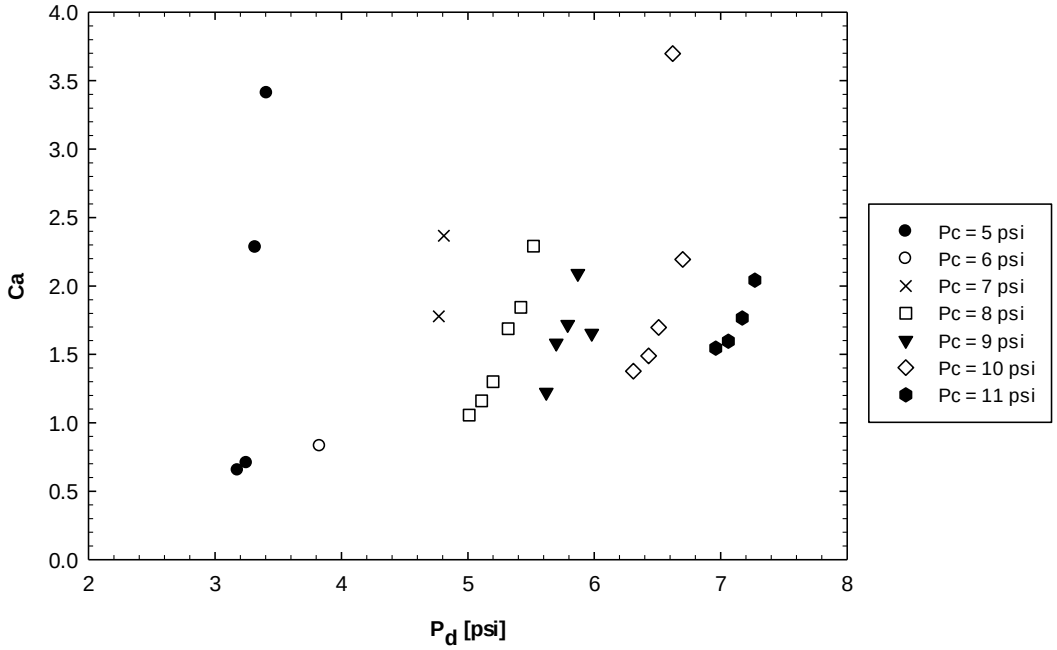

Figure 25 Dispersed pressure with the Capillary number of dispersed phase.

4.1.3 Modeling: circuit model for the flow-focusing geometry

The results above show that there is severe dependence of bubble size, velocity and frequency on the continuous phase pressure. They also show a relatively narrow range of pressures in which bubbles can be formed. Similar results have been reported previously [39, 40]. For example, Ward et al compared the flow-controlled system and the pressure-controlled system using oil and water as the fluids. They found that when the flow was driven at a specified flow rate (using a syringe pump); the drop sizes and frequency were only weakly dependent on the flow rates or relative flow rate. In contrast when the fluid pressures were specified with pressure regulators (similar to our experiments), the drop or the bubble size had a much stronger dependence on the pressure or relative pressure. They did not explain their observations in detail, but the key idea is

that each fluid must have some minimum pressure in order to penetrate into the junction. I.e. if the pressure of either fluid is too low, then its flow will stop altogether and drop formation will stop. This is the crucial difference between pressure-controlled flow as compared to flow-rate controlled flow: in the latter situation, it is possible to specify extremely low flow rates for either stream and still have bubble generation, whereas in pressure-controlled situations, a very low pressure on a stream will stop it' s flow altogether.

Here we will develop a simple model (Figure 26) that captures this idea quantitatively and explains both the flow map as well as the large dependence of drop size and frequency on the dispersed phase pressure. The basic idea is to draw equivalence between the fluid circuit and an electrical circuit with the flow rates being analogous to a current and the pressure drops being analogous to potential differences; each path then must have a resistance. Indeed, in single laminar flow situations (due to the low Reynolds numbers), the analogy can be made exactly since the fluid mechanical situation is linear (i.e. flow rates are proportional to flow drops). For multiphase flow situations (e.g. the drop flow from the junction to the exit), such linearity is not exact, but will be assumed here.

The model starts with defining the each portion of the flow path with a resistance as illustrated in Figure 26. A pressure of zero is ascribed at the exit, and a pressure of P_i is assumed at the junction. We will model the flow with three resistances instead of fours since the two continuous streams may simply be regarded as resistances in parallel. The results do not make any difference either with three resistances or four resistances; a four-stream circuit is equivalent to a three-stream with just double the value of R_c.

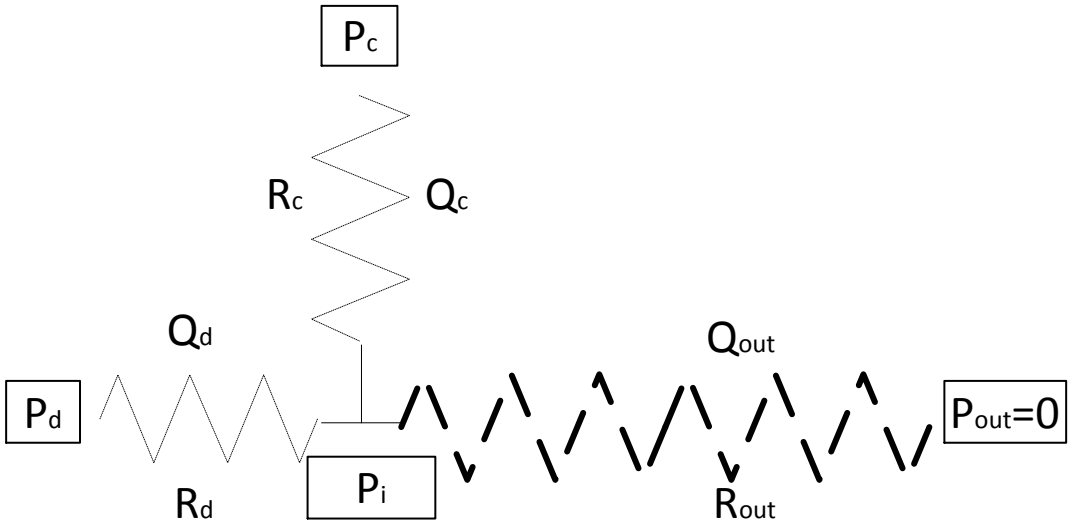

Figure 26 The scheme of pressure analytical method.

The relationship between the flow rates and the pressure drops along each path can be written by the following equations:

$$P_c - P_i = R_c Q_c \tag{16}$$

$$P_d - P_i = R_d Q_d \tag{17}$$

$$P_i = R_{out}(Q_c + Q_d) \tag{18}$$

where R_c, R_d, and R_{out} are the resistances of the channels, Q_c and Q_d are the flow rates, P_c and P_d are the pressure in the channels, and P_i are the pressure values in the intersection. As mentioned above, since the flow is laminar and single phase in the inlet channels, the above equations are exact and the R values can be calculated exactly from the geometry and viscosity. The R_{out} value corresponds to two phase flow and hence the linear relationship between pressure drop and flow

rate is only approximate. Ho and Leal [41] stated that exact pressure drop relationship can be calculated for cylindrical tubes from the viscosity ratio, the drop velocity, and the drop shape. Here we will not do so and the main conclusions from the model are not affected by this. Solving the above equations, the Q_c, Q_d and P_i could be calculated.

$$Q_c = \frac{-P_d R_{out} + P_c(R_d + R_{out})}{R_d R_{out} + R_c\,（R_d + R_{out}）} \tag{19}$$

$$Q_d = \frac{-P_c R_{out} + P_d(R_c + R_{out})}{R_d R_{out} + R_c\,（R_d + R_{out}）} \tag{20}$$

$$P_i = \frac{R_{out}(P_d R_c + P_c R_d)}{R_d R_{out} + R_c\,（R_d + R_{out}）} \tag{21}$$

Clearly, regardless whether bubble formation occurs or not, for obtaining forward flow of both fluids, both the Q values must be positive:

$$Q_c > 0;\ hence\ \frac{P_c}{P_d} > \frac{R_{out}}{R_d + R_{out}} \tag{22}$$

$$Q_d > 0; hence\ \frac{P_c}{P_d} > \frac{R_c + R_{out}}{R_{out}} \tag{23}$$

Accordingly, the forward flow is obtained in the limits: $Q_c = 0$; $\frac{P_c}{P_d} = \frac{R_{out}}{R_d + R_{out}}$ and $Q_d = 0$; $\frac{P_c}{P_d} = \frac{R_c + R_{out}}{R_{out}}$ that outside these limits, “back flow” will occur for one of the supply channels.

Clearly then, the flow map, i.e. the pressure range within which two phase flow (with or without bubble formation) can occur depends on the relative values of the three resistances. If the R_{out} is relatively small, the ratio of the inlet pressures can be significantly different from 1, whereas if R_{out} is large, two phase flow can occur only in a narrow range of pressure ratios. This

is illustrated in Figure 27 that shows two cases: one with all three resistances equal ($R_c = R_d = R_{out}$), and another when ($R_{out} = 15R_c$).

Next we turn to the actual values of the flow rates under conditions when two phase flow exists. The relationship of continuous flow rate Q_c, and the dispersed flow rate Q_d with dispersed pressure P_d are shown in Figure 28. This demonstrates when the continuous pressure P_c is fixed in is set to 10 (arbitrary units) and $R_c = R_d$, $R_{out} = 15R_c$ (also arbitrary units), with increasing P_d, Q_c decreases from a finite value to zero at a certain value of P_d. Conversely Q_d is zero at a certain value of P_d, and then rises linearly. This graph illustrates quantitatively the key idea expressed at the beginning of this section that there is a certain minimum pressure for each fluid to enter the junction.

Previous literature in flow rate controlled systems [24, 31, 39] suggests that size, frequency and velocity depend severely on flow rate when the one of the flow rates is very small. For example when Q_c is very small, very large bubbles are expected.

Li et al. [42] studied the empirical relations of bubble formation and they are able to quantitatively describe the phenomenon. Here, we describe our experiments from empirical correlations. The results of the experiment could lead us to predict the drop sizes based on theoretical models. According to Li's studies [42], the drop size as a function of the Q_d/Q_c ratio for various sizes of the gas inlet and gas-liquid outlet may be represented by the following correlation:

$$\frac{L}{W_g} = \beta\left(\frac{Q_d}{Q_c}\right)^{\alpha} \tag{24}$$

where the dimensionless ratio L/W is the bubble length to the channel width, and the power law index α and constant β. The relationship shows that the bubble sizes grow to infinity when the flow rate ratio is high. In contrast, the bubble size will be small when the flow rate ratio is low. It shows that size depends on flow rate ratio and therefore quantitatively, the circuit model predicts large pressure drop dependence, at least in the pressure region where one of the flow rates approaches zero.

$$V_{air} = \frac{Q_{air}}{Cross\ section\ area} \tag{25}$$

In the equation 25, the circuit model shows that the flow rate strongly depends on pressure, and there the velocity should depend as well. The velocity of dispersed phased will change significantly with the dispersed flow rate.

$$flow\ rate = Volume * frequency \tag{26}$$

Equation 26 indicates that frequency depends on the flow rate and the volume. The circuit model does not predict the volume. If volume is constant (i.e. drop diameter constant) then frequency will have same behavior as flow rate. In reality volume of drop increases with Q_d, and hence frequency does not increase as sharply with increasing P_d.

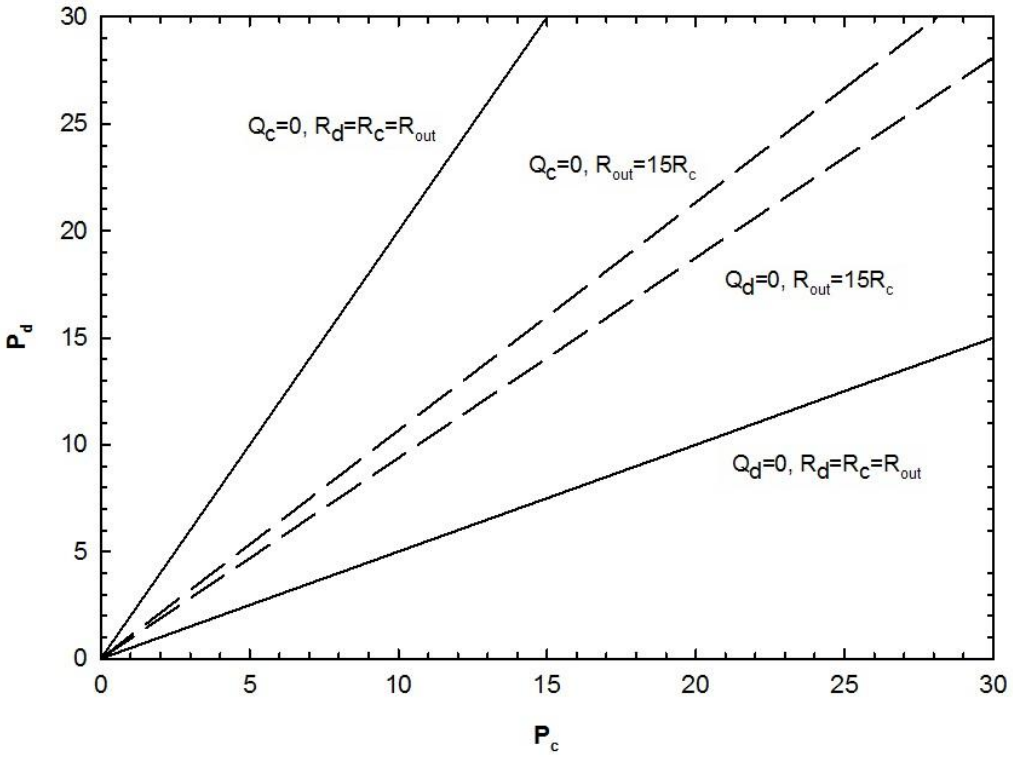

Figure 27 Pressure range in which forward flow occurs in all channels. The solid lines are calculated from equations 22 and 23 for $R_c = R_d = R_{out}$. The dashed lines correspond to $R_c = R_d$ and R_{out} is 15 times higher than R_c. Here the units of Pc and Pd are arbitrary.

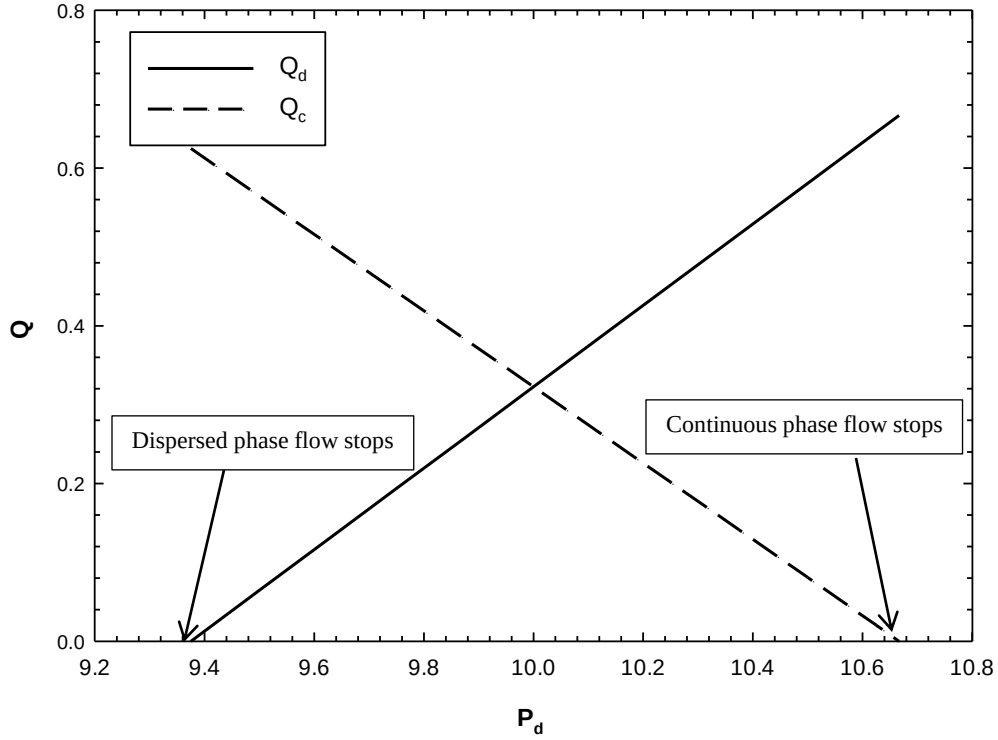

Figure 28 The dependence (calculated from equation 19-20) of the two flow rates on the dispersed phase pressure keeping the continuous phase P_c constant, The resistances here are $R_c = R_d$, $R_{out} = 15*R_c$

Having established the reason for the strong pressure dependence qualitatively, we now test the model more quantitatively. We assume R_d is much smaller than R_c because the viscosity of nitrogen gas ($17.8*10^{-6}$ Pa.s) is far lower than of the PDMS fluid (30 Pa.s). Therefore we will simply set R_d to be zero. Equation 20 therefore becomes:

$$Q_d = \frac{-P_c}{R_c} + \frac{P_d}{R_c}\left(\frac{R_c}{R_{out}} + 1\right) \qquad (27)$$

This equation has two fitting parameters, R_{out} and the ratio R_c/R_{out} which can be adjusted to fit the Q_d vs. P_d data of Figure 23. The fit (done by eye) is shown in Figure 30. It is clear that the same values of fitting parameter can capture the data at all values of P_c simultaneously. This lends confidence to the validity of the circuit model. The actual values of the fitting parameters are R_c/R_{out} = 0.6, R_c = 9.7*10^{-9} $\frac{\text{Psi.s}}{\mu m^3}$ and R_{out} = 1.6*10^{-8} $\frac{\text{Psi.s}}{\mu m^3}$. We may estimate the value of R_c and R_{out} using the equations for laminar flow in for the rectangular channel flow [43]:

$$R_i = \frac{\alpha \mu L}{w^2 h^2} \tag{28}$$

$$C = \frac{4(h + w)^2}{h * w} \tag{29}$$

where L is the channel length, w is the channel width, h is the channel height, α is the geometrical correction factor, and C is dimensionless compactness. According to the Figure 29 [43], we could find the C and α for the rectangular flow. Here, we combine the channel resistance in sequence because of the complicated geometries. The continuous phase resistance is combined the two acrylic supplied channels with vertical channels, R_c = 4.7*10^{-9} $\frac{\text{Psi.s}}{\mu m^3}$. And outlet resistance is combined the constriction channel with the downstream channels, R_{out} = 4.1*10^{-8} $\frac{\text{Psi.s}}{\mu m^3}$. The ratio of R_c/R_{out} = 0.1. The absolute values of R_c and R_{out} obtained experimentally are within a factor of 4 of the values estimated. However, the calculated ratio is in poor agreement with that calculated theoretically.

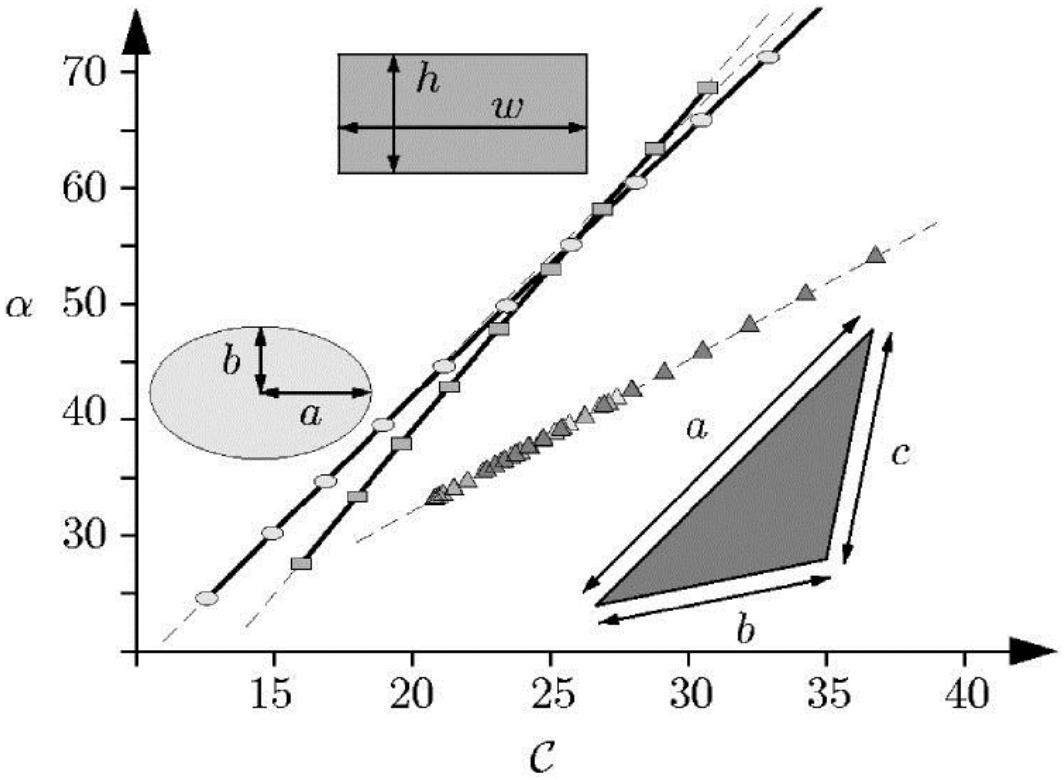

Figure 29 The correction factor versus compactness for the elliptical, rectangular, and triangular classes. Numerical results from a finite-element simulation are also included (○, △, and □) Reprinted with permission from the authors [43].

These are predictions for the combination of P_c vs. P_d in which forward flow is obtained. It is clear that the lower limit (i.e. the minimum pressure needed for bubble formation) is well-captured by the model. The upper limit cannot be measured experimentally since we stop the flow experiments when bubble generation transitions into tubing flow. Thus experimentally we are not able to determine whether the predicted limit for when the air will start backing up the PDMS supply channels is accurate or not.

In summary, the circuit model which ignores all surface tension phenomena, is able to predict the flow characteristics of the two-phase flow, and furthermore is able to qualitatively explain why the drop size depends strongly on the dispersed phase pressure.

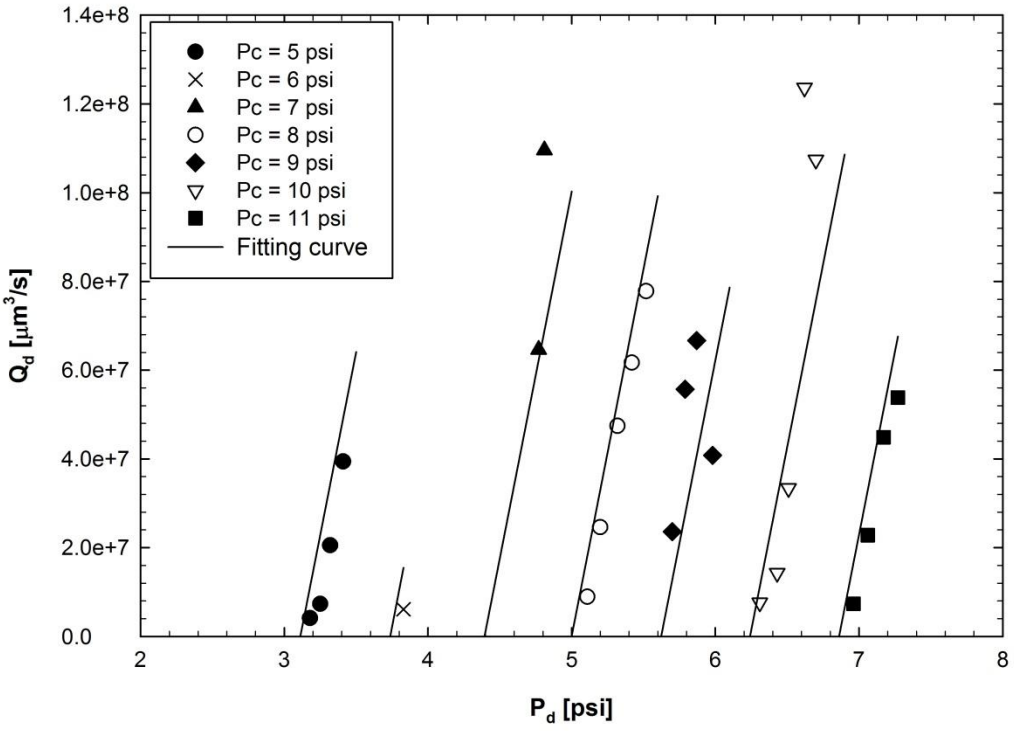

Figure 30 Approximate fits of equation 27 to the flow rate vs the dispersed phase pressure.

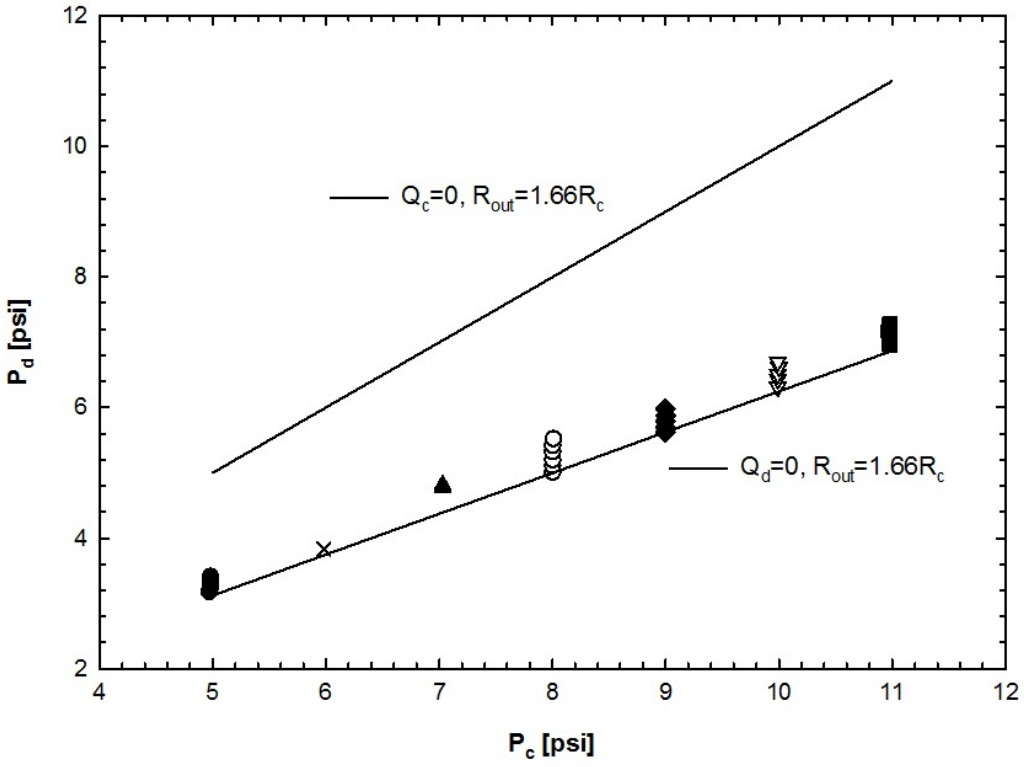

Figure 31 The flow map from equation 22-23 using the same value of R_{out}/R_c as obtained from the previous figure ($R_{out}=1.66R_{c)}$.

4.1.4 Effect of viscosity of the continuous phase

To study the effect of viscosity of the continuous phase, we used three different viscosities, 10K 30K and 500K, of PDMS fluids. Figure 32 shows the flow map with different viscosities of the continuous phase fluids. Figure 33 shows that the bubble size decreases somewhat as the viscosity of the continuous phase increases, nevertheless, the bubbles remain comparable in size

to the device dimensions. Comparing the three viscosities at the same pressure values, Figure 34 illustrates that the velocity of the bubbles decreases significantly as the viscosity of the continuous phase increases. Figure 36 show the frequencies of the bubble formation reduce as the viscosity of the continuous phase PDMS increases. Finally, the flow rate of the continuous phase, obtained as the product of the bubble volume and the frequency, is illustrated in Figure 38. The increase in continuous phase viscosity reduces the bubble flow rate. We will now consider each of these in turn.

The bubble size itself does not appear to change suggesting that it is primarily determined by the geometry of the junction. Indeed the basic theory of drop breakup states that drops are formed when the capillary number reaches its critical value of 1

$$\mathrm{Ca}_{crit} = \frac{F_{viscous}}{F_{surface}} = \frac{\mu v}{\gamma} = 1 \qquad (30)$$

Since bubble size does not appear in this equation, the weak dependence of bubble size on flow conditions is not surprising.

Next we turn to the flow rate. The circuit model predicts that flow resistances are proportional to viscosity and hence flow rate should be inversely proportional to viscosity. This scaling is tested in Figure 39 which plots the product of viscosity and flow rate vs. P_d. While the data do not collapse into a single curve, they do fall in a somewhat narrow band suggesting that to a first approximation, the bubble flow rate reduces because the viscosity increased.

Next frequency can simply be found from the time required to create a drop of the desired diameter at the flow rate available. Since drop size does not change much, and Q is inversely related to viscosity, frequency must reduce with increase in viscosity. Indeed this is seen as well.

Next we turn to the velocities and frequencies. Figure 35 and Figure 37 show that both these quantities scale with the viscosity, i.e. the product frequency*viscosity or velocity*viscosity cause the data to collapse indicating that velocity and F are both quantities are proportional to viscosity. The flow rate Q_d also shows this phenomenon. The flow rate is affected by the drop volume and the frequency. Thus, in different viscosities fluids, the flow rated would only affected by the frequency. The result in Figure 39 demonstrated the rescaled effect on the flow rate. According the circuit model we developed above, the flow rate is a function of pressures and resistances. As viscosity increases, resistance increases. So flow rates go down. Since drop size does not change much, frequency goes down. And the bubble velocity is the function of the flow rate. That's why the velocities decrease with the increase of the viscosity.

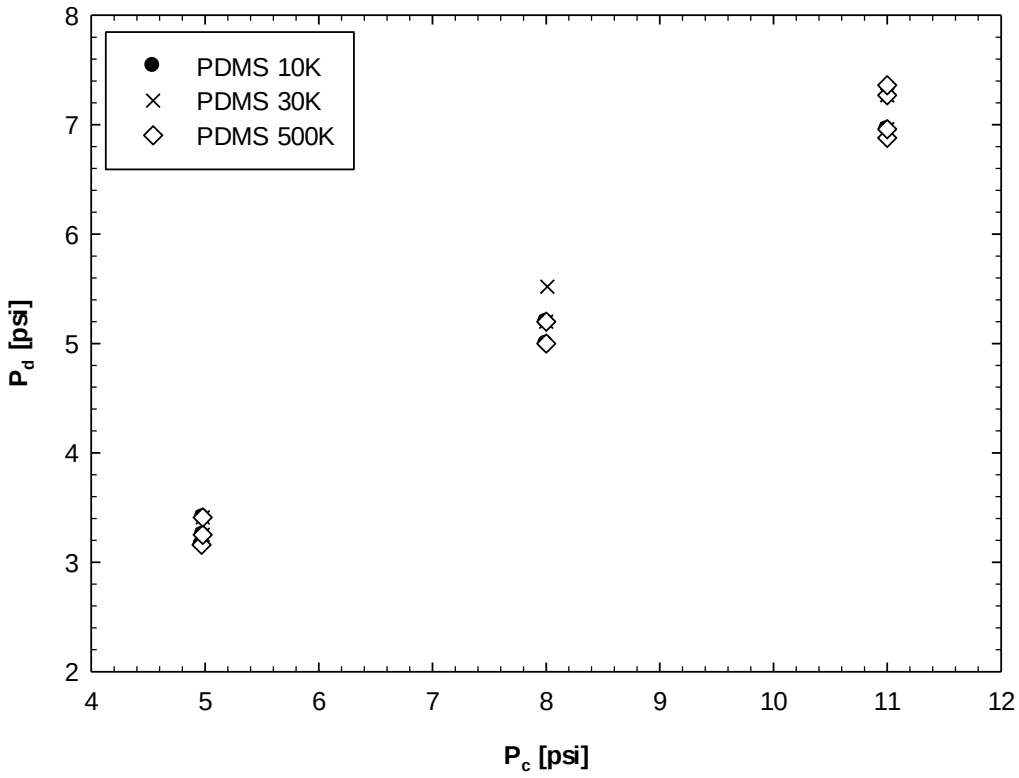

Figure 32 The combinations of continuous fluid pressure (P_c) and dispersed fluids pressure (P_d) at different viscosities.

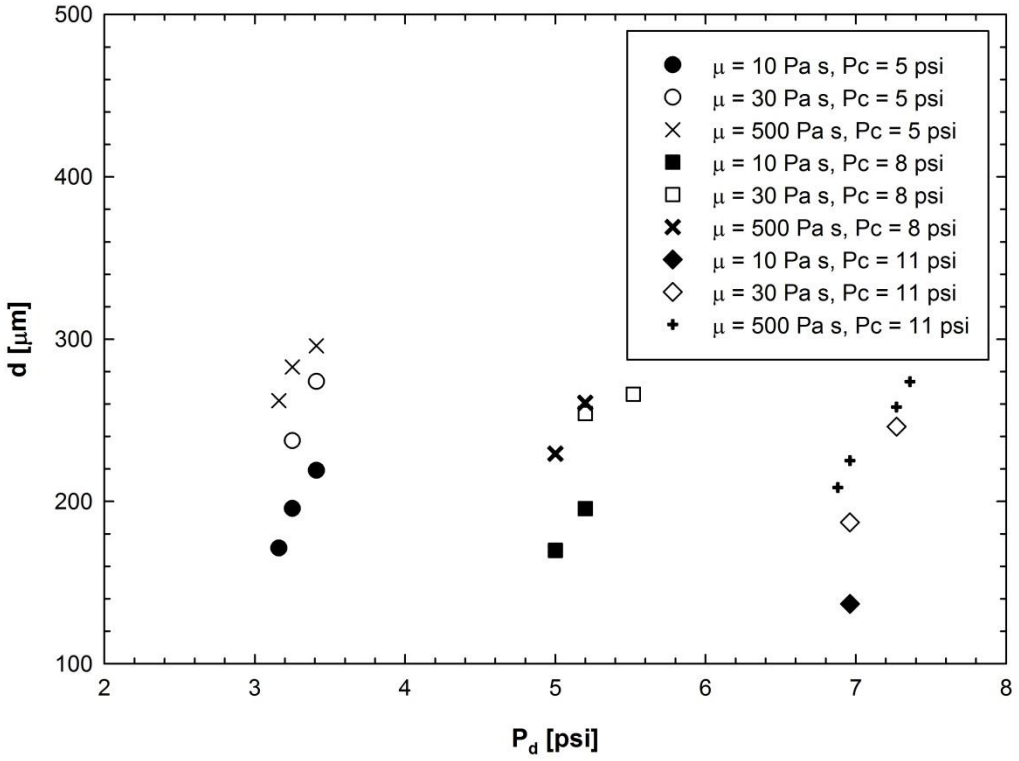

Figure 33 Effect of continuous phase viscosity on bubble sizes.

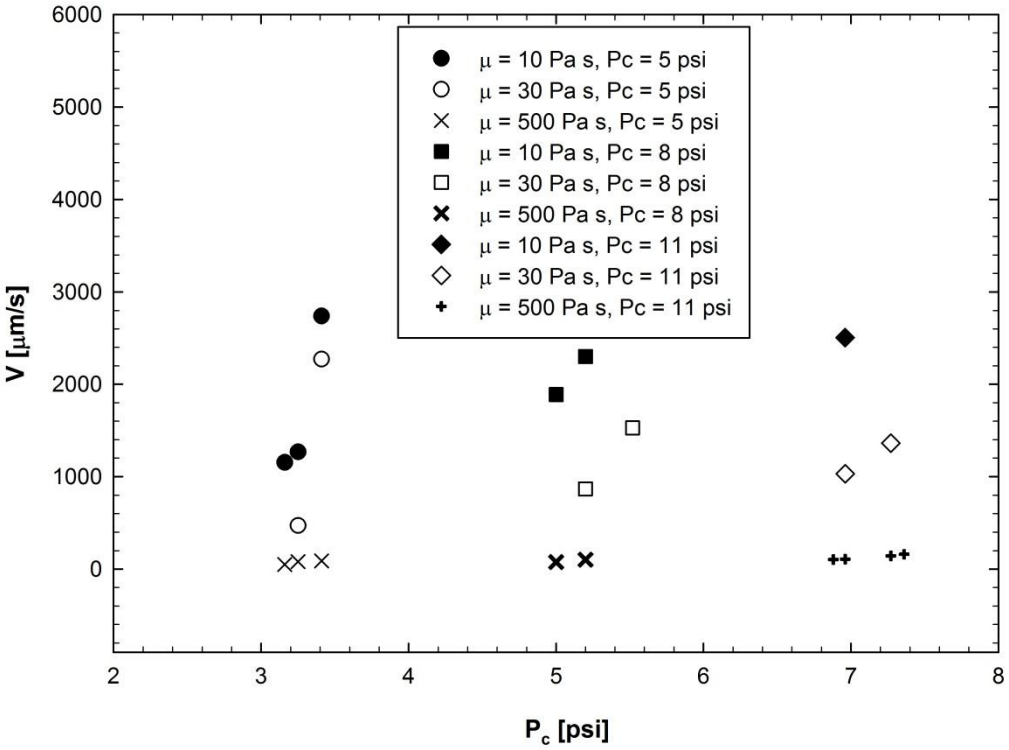

Figure 34 Dependence of drop velocity on the viscosity of the continuous phase.

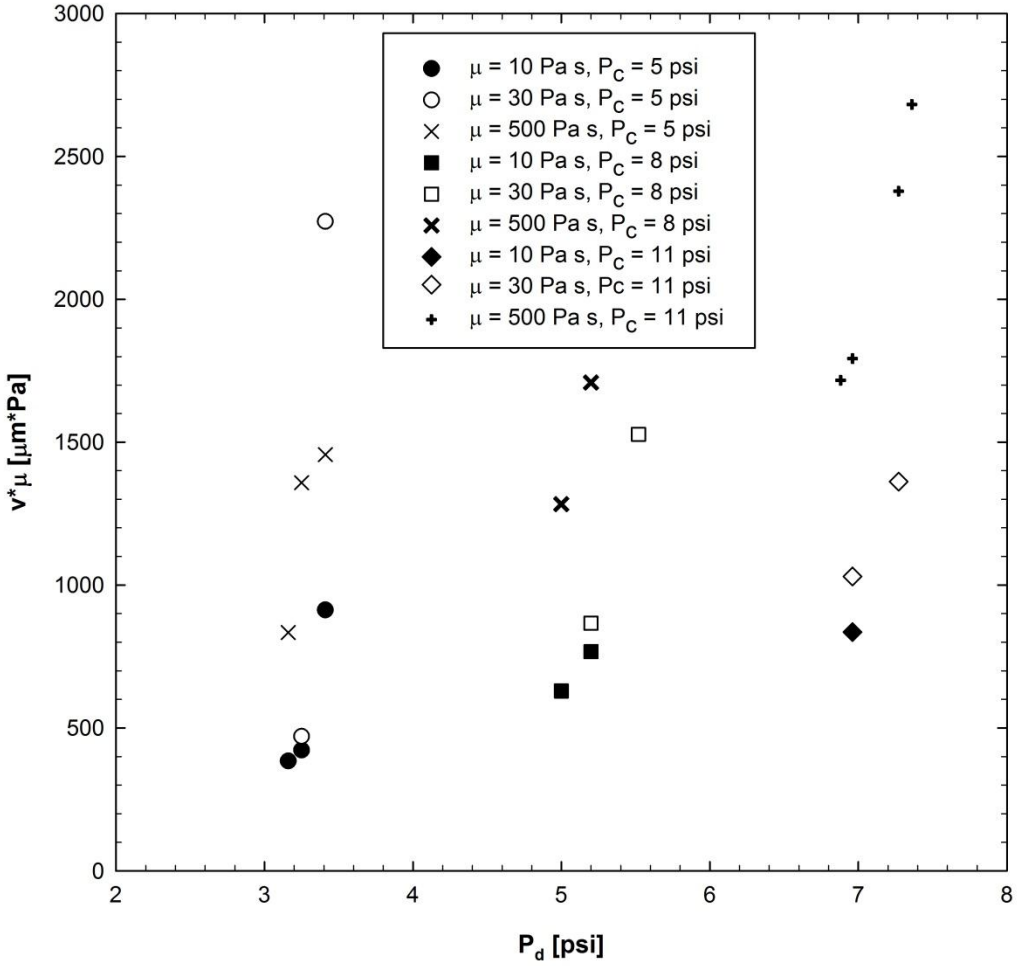

Figure 35 The velocity shifted by velocity* viscosity.

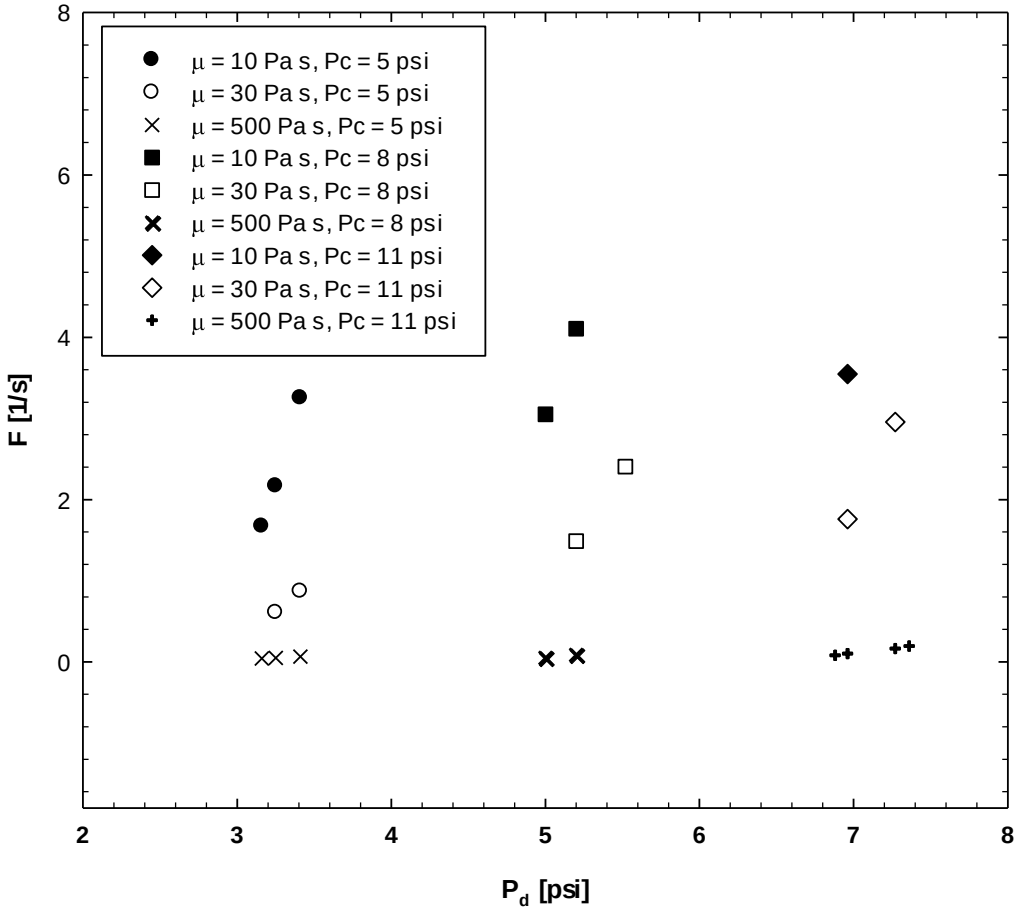

Figure 36 The drop frequency in different viscosities. The frequency goes up when the P_d increases. In addition, the highest viscosity continuous phased fluid gets the lowest frequency.

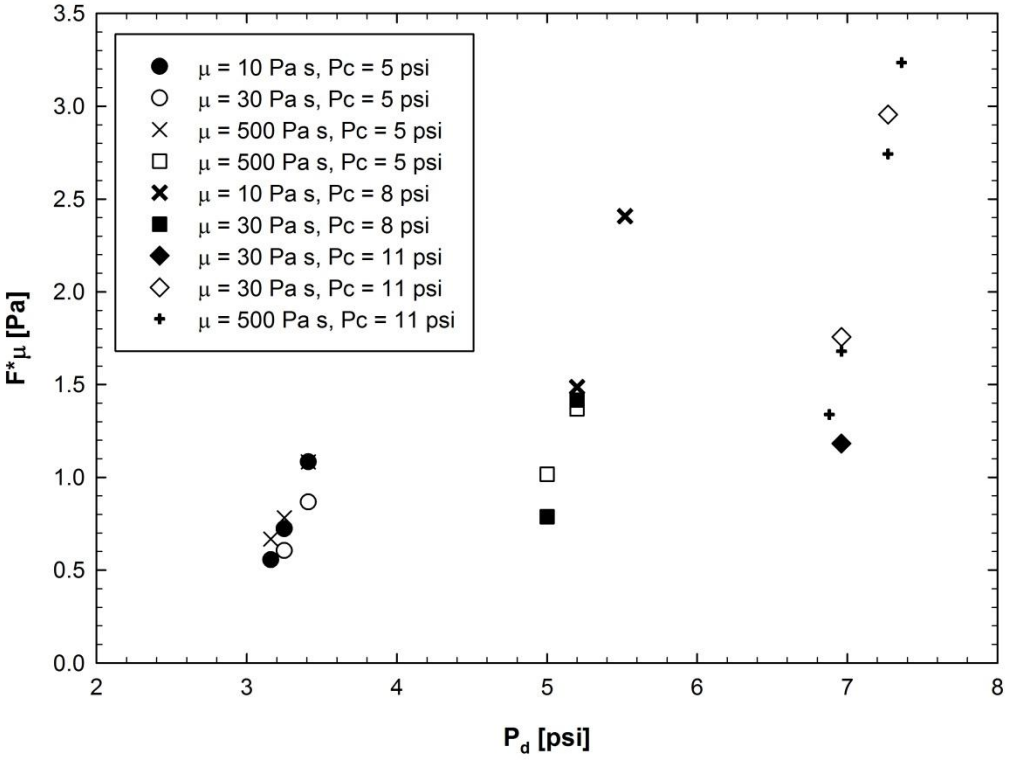

Figure 37 The frequency shifted by frequency* viscosity.

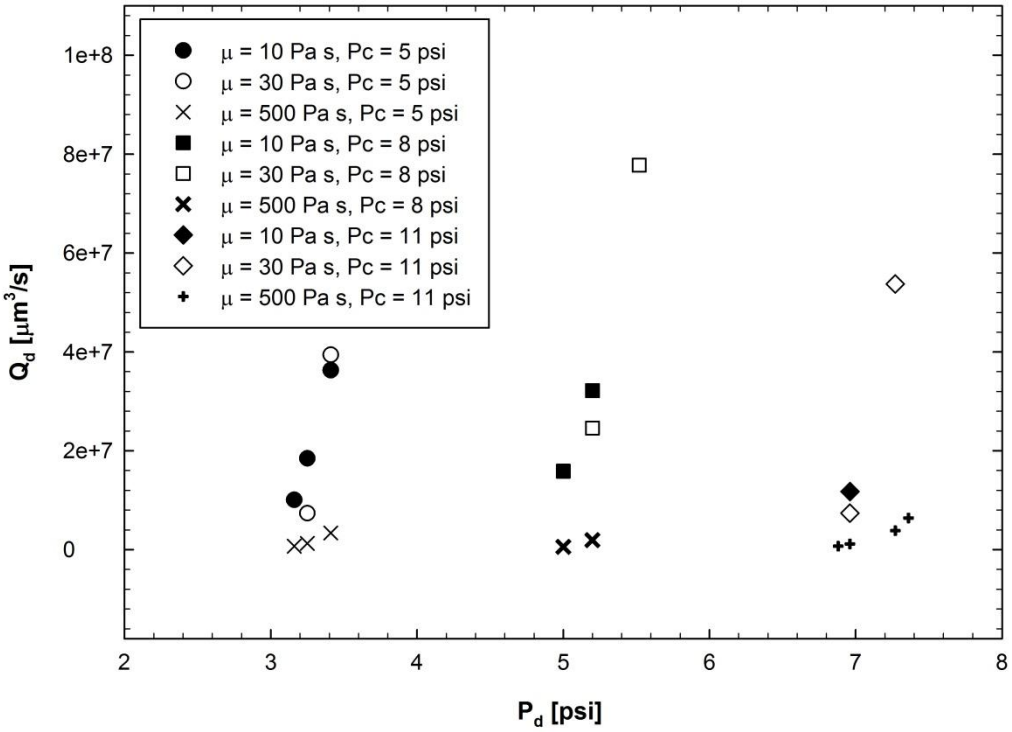

Figure 38 The flow rate Q_d in different viscosities. The frequency goes up when the P_d increases. In addition, the highest viscosity continuous phased fluid gets the lowest Q_d. The Q_d axis is plotted in the log scale.

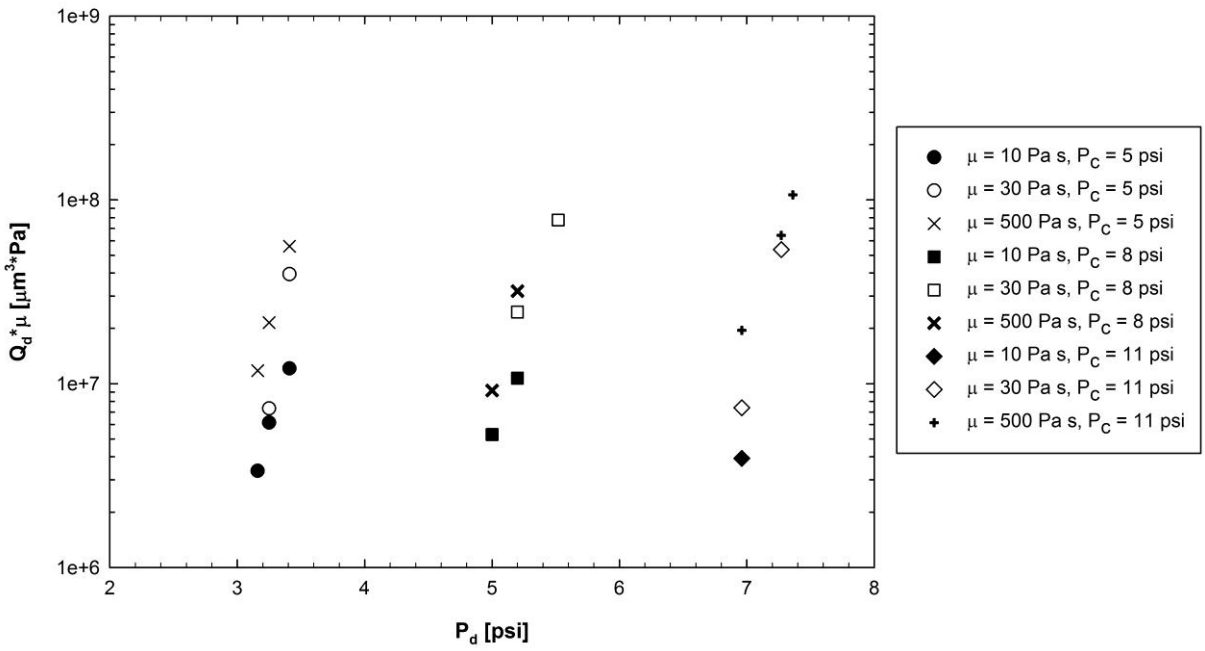

Figure 39 The flow rate Qd shifted by Qd* viscosity. The Q_d axis is plotted in the log scale.

5.0 LIQUID-LIQUID SYSTEM

The previous chapter tested out the feasibility of bubble formation in a pressure-driven microfluidic device with a highly viscous continuous phase. Those experiments give some confidence that interfacial tension-driven drop breakup can still occur with undiluted polymer melts; thus in principle, molten polymer microfluidics is feasible. We now turn to examining a liquid/liquid system where both the continuous as well as dispersed are both undiluted polymeric liquids. As before, both fluids are high-viscosity liquids at room temperature. In the flow-focusing microfluidic device, the drop formation is qualitatively different from the bubble. Two-phase liquid flows in microfluidic devices have been widely studied [24, 44, 45]; however, there are no reports of generating drops from undiluted molten polymers.

5.1 EXPERIMENTAL PROCEDURE

The continuous phase was PDMS 100k which has a viscosity of 100 Pa.s. The dispersed phase liquids are liquids of various viscosities: water, PEO400, PI. The experimental protocol is the same as before: keep P_c fixed while increasing (or reducing) P_d in a stepwise fashion. The continuous phase liquid and the dispersed phase liquid are both filled into the reservoirs at the

same time, and then the continuous phase liquid is filled into the channel first to prevent the wetting problem. In early experiments with the three layer shims, we noted problems with wall wettability: sometimes the dispersed phase fluid would touch the bottom and/or top wall and leave a residue that interfered with the imaging and complicated further experiments. Following Figure 13, the dispersed phase fluid can be prevented from touching the top and bottom wall by simply making the top and bottom shim layer thicker; this was done with two additional shims of thickness 125 μm at the top and bottom. This five layer device prevented the wettability problems in the liquid/liquid experiment.

The remainder of the experimental apparatus and procedures were identical to those in the previous section. However as we discussed below, an entirely different behavior was found.

5.2 RESULTS

We had expected that, similar to the formation of bubbles in the previous chapter, we would be able to form droplets could be formed at the cross-flow junction. Thus the original goal of the experiments was to examine the similarities and differences between the quantitative behaviors, e.g. drop vs. bubble sizes, the range of pressures in which drops can be formed, etc. However, in the present case, the dispersed phase PI was found to form a continuous filament, rather than breakup into drops. The formation of this thin filament is shown in Figure 40 and Figure 41.

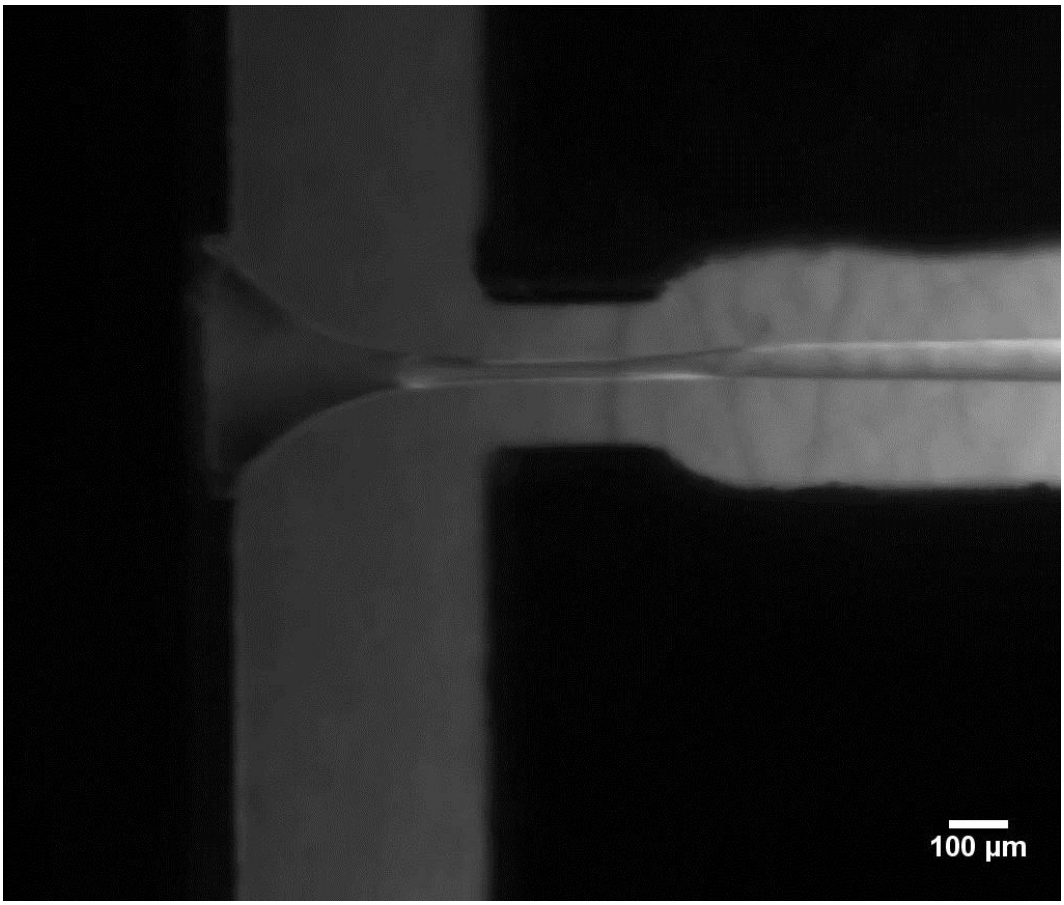

Figure 40 Formation of a PI filament surrounded by continuous phase PDMS. P_c = 5 psi and P_d = 2.61 psi.

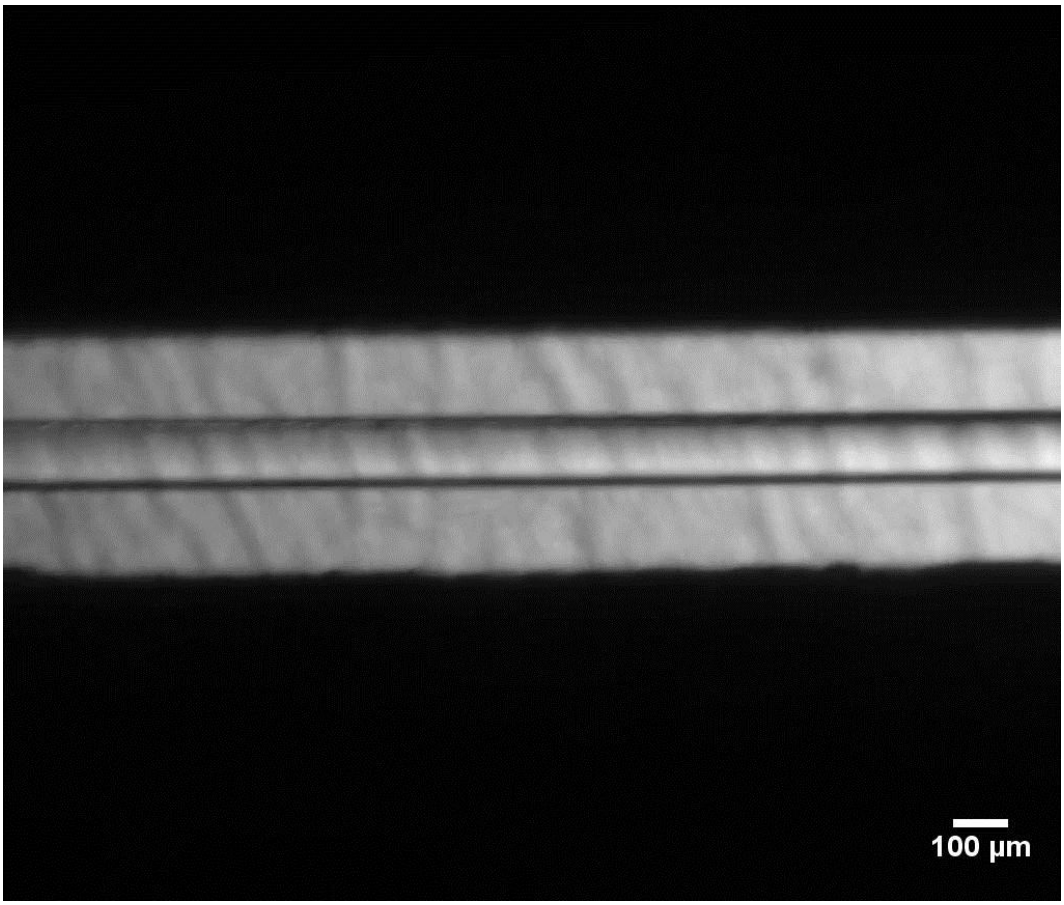

Figure 41 The downstream image of the filament of PI surrounded by continuous phase PDMS. P_c here is 5 psi, and P_d is 2.61 psi.

At high values of P_d, this filament was stable and was convected downstream to the exit of the device. As the P_d was reduced, the thickness of the thread was found to decrease. Sufficiently thin filaments eventually broke by a downstream capillary instability into a string of drops as illustrated in Figure 42. Between the primary drops in this string, smaller satellite drops are clearly visible, and this has been noted commonly in capillary breakup phenomena. These drops were then convected to the exit of the channel. The drops formed by this downstream

capillary breakup are far smaller than the gas bubbles formed in the cross-flow junction in the previous chapter, and indeed. Indeed, the gas bubbles were comparable in size to the dimensions of the channel, whereas the drops of Figure 41 are many times smaller than the smallest dimension (the 127 micron constriction) of the channel. This observation is potentially useful since it raises the possibility of creating polymeric particles that are far smaller than the size of the microfluidic channels.

Figure 43 shows the flow map of the combinations of pressure within which different thickness of the threads can be generated. The qualitative behavior is similar, the bubble size or the thread size increased with the higher P_d, however the actual pressure values at which two-phase flow occurs is different, perhaps due to the change in overall thickness of the flow geometry.

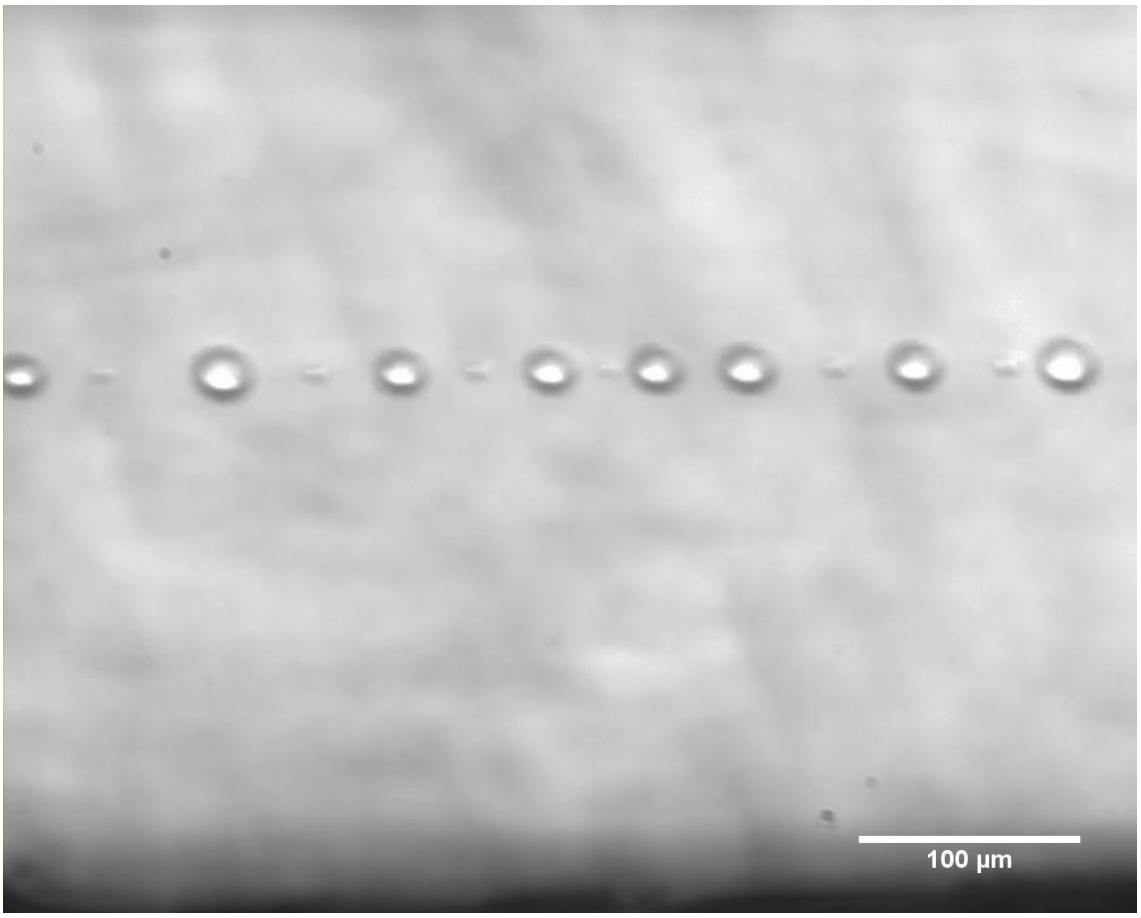

Figure 42 A string of PI drops formed downstream of the crossflow junction by a capillary instability of a PI filament.

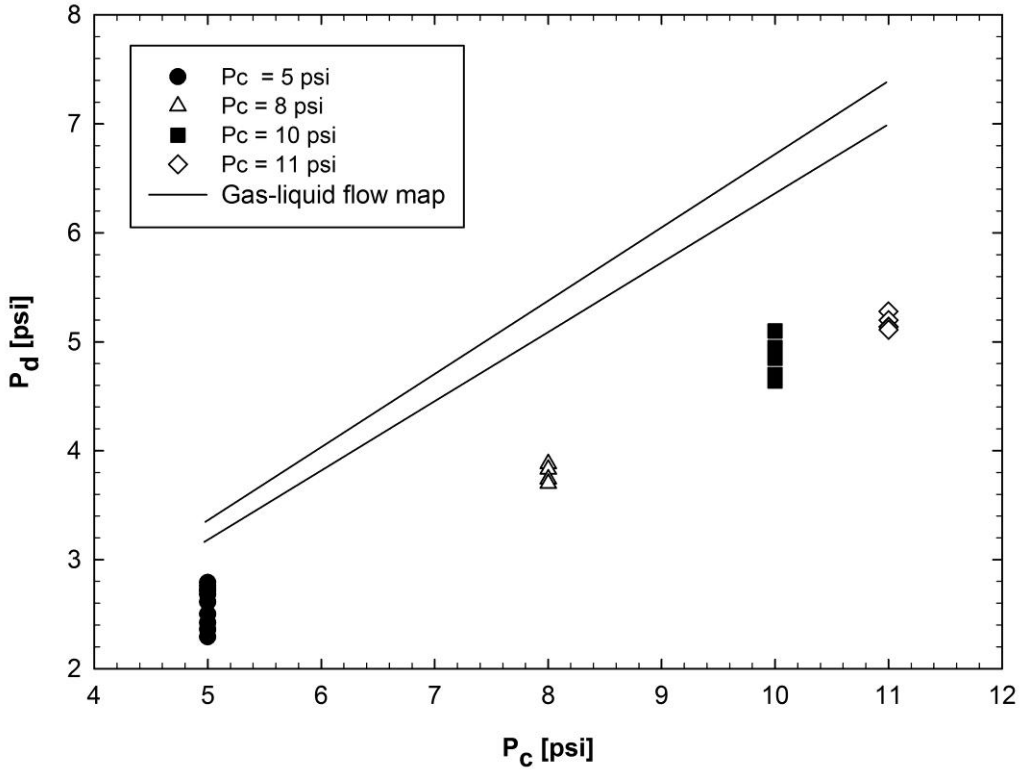

Figure 43 The pressure flow map of the PI dispersed phase flow.

The diameters of the filament are shown in the Figure 44 as a function of the dispersed phase pressure. Similar to the behavior of the bubble sizes in the previous chapter, there is a significant dependence of the filament diameter on the pressure. The filaments that show capillary breakup correspond to the lowers value of P_d at which two-phase flow is still possible; in this region, there is a strong decrease of filament diameter. This suggests that the capillary breakup may occur only because the dispersed phase flow is on the verge of stopping, leading to very small filament diameters and possible small fluctuations in diameter, both of which facilitate capillary breakup.

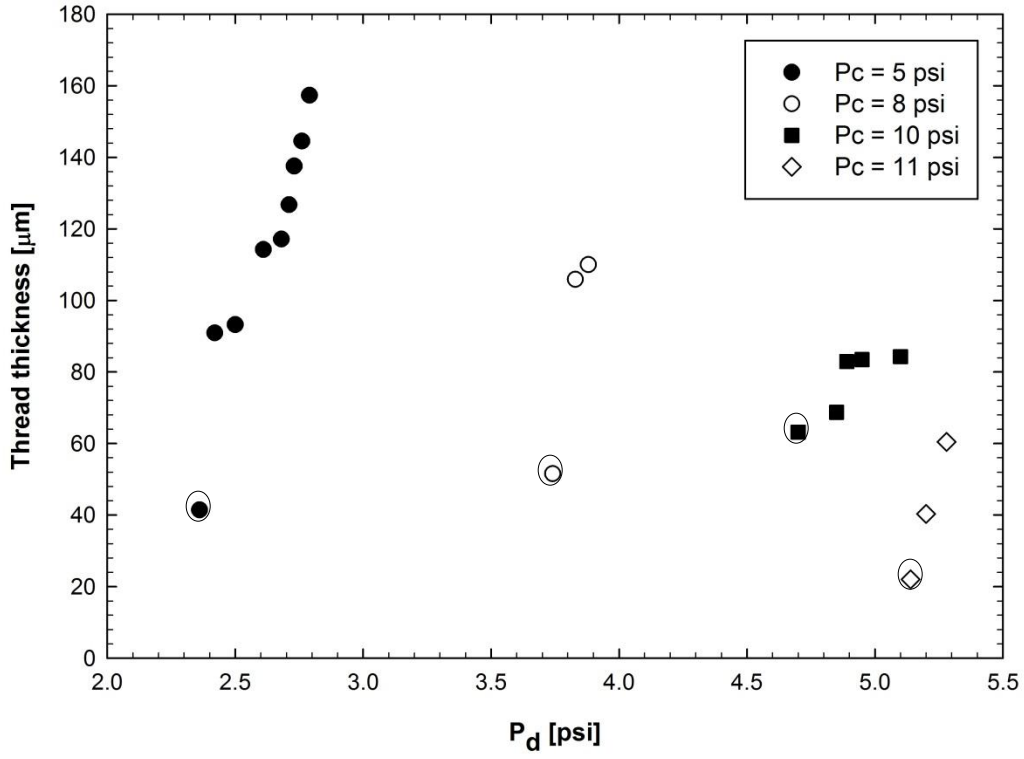

Figure 44 The diameter of the PI filament as a function of dispersed phase pressure. The points shown with a circle showed a downstream capillary breakup similar to that shown in Figure 42.

5.3 DRIPPING VS. JETTING

The chief result of this chapter is that the behavior of the PI/PDMS flow is altogether different from that of the air/PDMS flow. We seek to examine the reasons for this change. At least three possible reasons may be listed for this difference: compressibility, viscosity ratio, and interfacial tension, and each of these will be considered in turn.

Drop breakup is induced by interfacial tension. Indeed in Chapter 2, we discussed the role of capillary number ($\eta v/\sigma$) and noted that breakup is possible only if the capillary number is relatively small. At large value of capillary number, continuous stream flow was observed as illustrated in Figure 4. The surface tension of the Nitrogen gas/PDMS interface may be expected to be about 19 mN/m [46] whereas that of the PI/PDMS interface may be expected to be about 2.73 mN/m [46]. Clearly the lower interfacial tension between PI and PDMS may raise the capillary number and make the breakup more difficult, but it doesn't affect too much compared to viscosity ratio. The second is that air is compressible whereas PI is not; this may play a role in the breakup. Thirdly, the viscosity ratio changes from $1.781*10^{-7}$ for the Nitrogen gas/PDMS experiment to 1.3 for the PI/PDMS experiment; this may also influence breakup phenomena. Additional experiments were conducted to test these possibilities.

Table 2 Viscosities ratio and surface tension between liquids

Fluid	Viscosity Raito	Surface tension (mN/m)
Nitrogen gas/PDMS 100K	$1.781*10^{-7}$	19
Water/PDMS 100K	10^{-5}	34.8
PEO-400/PDMS 100K	$1.08*10^{-3}$	3-12 [2]
PI (LIR30)/PDMS 100K	1.3	2.73

[2] typical of polymer pairs

In order to test the effect of dispersed phase compressibility, the experiment was repeated using water as the dispersed phase, and keeping the same PDMS 100K as continuous phase. The viscosity ratio for water/PDMS is 10^{-5} as compared to $1.781*10^{-7}$ for Nitrogen gas/PDMS. While these are not equal, they are both far less than 1. Furthermore, the viscosity ratio of interfacial tension between water and PDMS is 10^{-5}, which is even higher than air/PDMS; thus replacing air with water is not likely to increase the capillary number. Thus it is reasonable to expect that any difference between the flow behaviors of the air/PDMS pair vs. the water/PDMS pair would be attributed to difference in the compressibility. In fact our experiments show that their behavior was qualitatively similar (Figure 45) and water drops could be generated similar to the air bubbles. This experiment definitively suggests that compressibility is not the reason for the difference between PI and air.

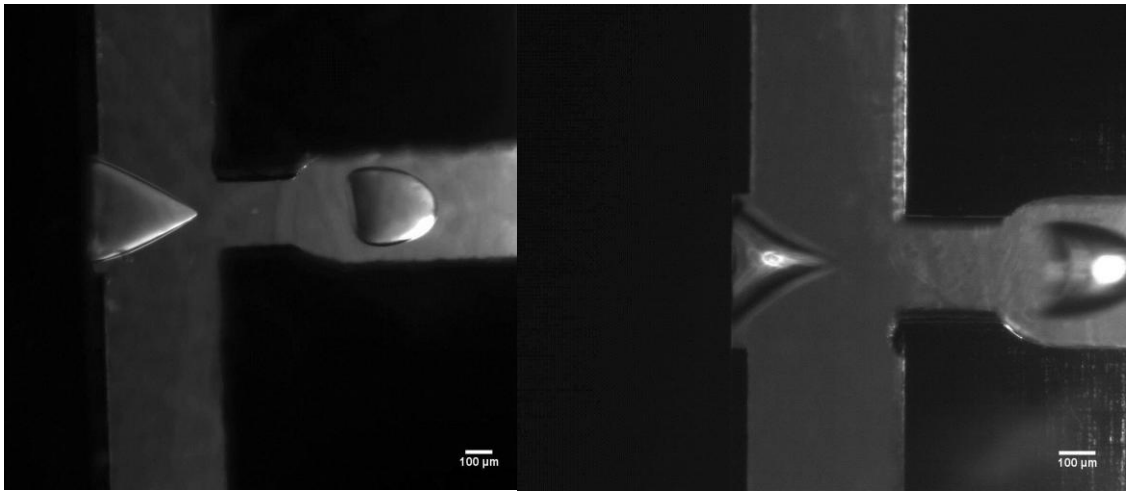

Figure 45 A: the water droplet formation B: the Nitrogen gas bubble formation. Give information on pressure.

Next we turn to the viscosity ratio. The hypothesis is that as viscosity ratio increases, at some value between 10^{-5} (for water/PDMS) and 1.3 (for PI/PDMS) a there will be a change in behavior from drop formation at the cross-flow junction (usually called dripping) to either filament formation (usually called jetting). The first fluid considered was PEO 400 with a viscosity of $90*10^{-3}$ Pa.s, corresponding to a viscosity ratio of $9*10^{-4}$. The behavior is shown in Figure 46 and it is clear that PEO400 forms a short thread to break up instead of downstream break up. Thus the reason for the difference between the air/PDMS and the PI/PDMS appears to be attributable to the viscosity ratio: it appears that with increasing viscosity ratio, there is a transition from dripping to jetting (with downstream breakup) to jetting that forms a filament that does not breakup readily.

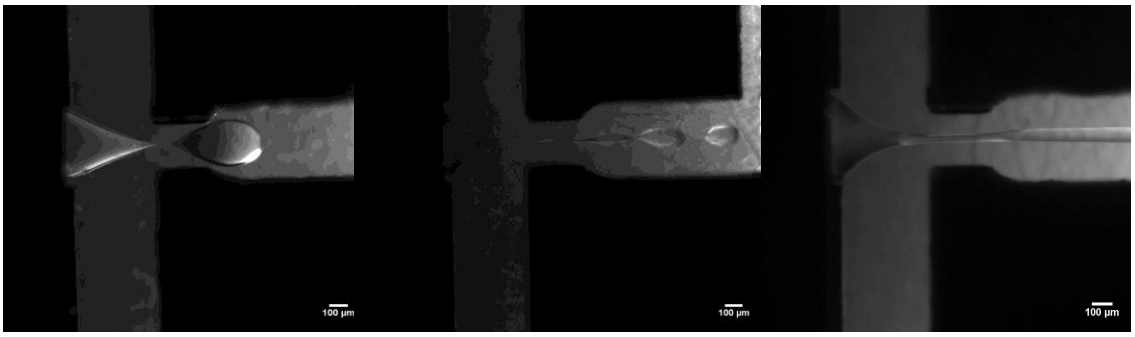

Figure 46 A: drop formation in the cross-flow junction for water. B. Formation of a short filament with downstream breakup with PEO400. C. Formation of a filament without downstream breakup. The continuous phase fluid here is PDMS 100K. P_c here is 10 psi, P_d is 4.73 psi.

This idea that the viscosity ratio can affect the dripping to jetting transition has been explored in the literature, albeit in flow rate controlled devices (rather than pressure-controlled

devices). The previous literatures show the results that when the velocity of the liquids is fixed, the more stable stream is obtained with the viscosity of the liquid increased [37, 44, 45, 47].

To summarize the results of this chapter, switching from air/PDMS to PI/PDMS requires increasing the thickness of the top and bottom layers so that the dispersed phase fluid does not contact the top and bottom walls. The chief result is that there is a qualitative difference in behavior: switching from air to a higher viscosity fluid result in the formation of a thin filament. If this filament is made sufficiently thin, it is possible to induce downstream breakup; this has the potential advantage of forming drops that are significantly smaller in size than the channel dimensions. However in this device at least, there was only a very narrow range of conditions in which downstream breakup was observed. We presume that this is because the diameter of the filament generated is relatively large, and the time required for capillary breakup is so large that the filament exits the device before breakup can occur.

We considered one approach for accelerating downstream breakup, viz. perturbing the filament diameter with the goal of reducing the time required for inducing the capillary instability. The basic idea was to perturb the value of P_d at a certain frequency so that the filament would develop slimmer "necks" at regular intervals; these necks would then be sites where the capillary instability could occur rapidly.

We built up a three way solenoid valve system (Figure 47) to test if we could increase the perturb of the dispersed phase stream. Two different dispersed phase pressure were provided by two independent regulators, and the solenoid valve could switch rapidly so that the dispersed phase pressure could be alternated between two values. By controlling the frequencies of the

switching valves, we could create a square-wave pressure signal to vary the dispersed phase flow rate.

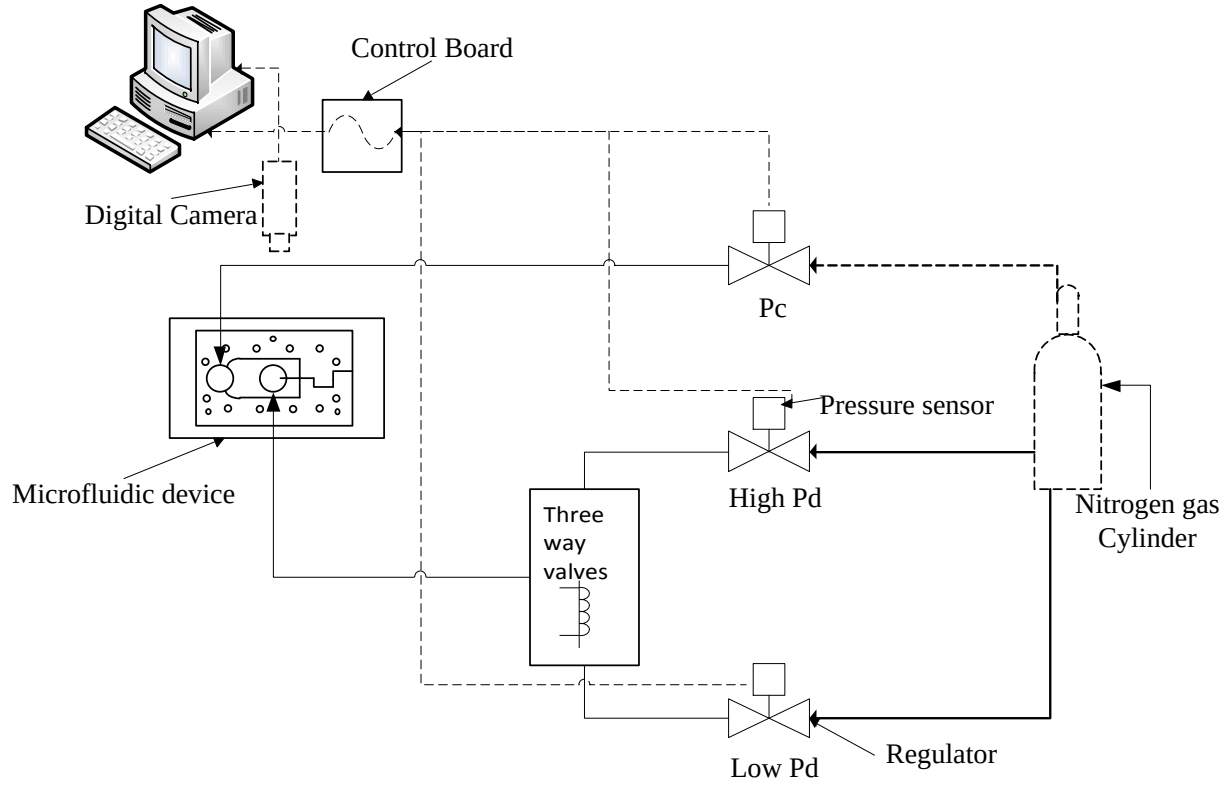

Figure 47 The solenoid system includes three regulators, a solenoid valve. The solenoid could be switched between the high P_d and low P_d.

Experiments were conducted with P_c = 10 psi. The value of the P_d was oscillated between two values that differed by as little as 0.4 psi (solenoid switching between 5.2 psi and 4.8 psi) to as high as 7.5 psi (solenoid switching between 8 psi and 1.5 psi). The frequency of oscillations was varied from 0.1 Hz to 1.5 Hz. In all these cases, it was found that while we could perturb the filament substantially, the perturbation was still insufficient to induce breakup while the filament was still within the device. We did see downstream breakup in many circumstances; however,

this was invariably when the filament diameter was already very small. Thus the chief conclusion was that downstream breakup is possible only if sufficiently small diameter filaments can be generated.

Appendix A shows preliminary results using substantially smaller micro-channels in which filaments of small diameter can be realized readily. In those cases, downstream breakup was observed in a wide range of parameters.

6.0 CONCLUSION AND FUTURE WORK

6.1 CONCLUSION

In this study, our two major problems, (1) high viscosity and low interfacial tension makes it difficult to break a continuous fluid stream into drops (2) high viscosity and high temperature required completely new methods of fluid handling, are discussed and resolved. By developing the pressure-driven system and metal shims for microfluidic channels, we can solve the wetting problem and high viscosities issues for the development of molten polymer microfluidics.

In the gas-liquid experiment, we demonstrated the circuit model to explain the fluid phenomena in the micro channels. By discussing the bubble sizes, flow velocity, flow rate, frequency, and different viscosities fluids, we find that (i) the flow rates are the functions of the pressure in the channels and the resistances of the channels. This model could explain why the bubble size depends severely on the pressure driving the flow (ii) The frequency of the bubbles is increased with the increase of $P_{d.}$ (iii) the different viscosities fluids do not affect the bubble sizes but flow rate, velocity, and frequency.

In the liquid-liquid experiment, we note that for the high viscosity dispersed fluid, the dripping phenomenon is not observed, instead, threading and jetting were obtained. From the different viscosities dispersed fluids test, we could conclude that this threading phenomenon is not caused

by the compressibility of the dispersed phase, but by the viscosities difference between the dispersed fluid and the continuous fluid.

At the beginning of this work, we did not have confidence that we could form drops with molten polymers at all. Now that we have done this, we are certain that we can get polymeric drops by downstream breakup.

6.2 FUTURE WORK

The results of the liquid-liquid system suggest narrowing down the size of the microfluidic channels to test whether we can reliably generate drops with a downstream breakup. We have made anther device for the high temperature experiment. The dimension of the constriction is narrowed down to 75 micron, which helps us to decrease the drop sizes. In this device, still operating with the same fluids and at room temperature, we are able to make 10-20 micron sizes droplets. The details of this experiment are attached in the appendix A. The high temperature device was fabricated by a Mechanical Engineering Design team as a part of an undergraduate design class. The experiments in the Appendix were conducted with assistance from undergraduate researcher Justin Lowen.

Accordingly the future direction of this work is towards testing a wider variety of polymers that are not liquid at room temperature. This would require the device to operate at high temperature to form molten polymer drops, but then also cool them rapidly to solidify them into particles.

Finally, it would be useful in the future to explore the formation of particles with complex geometries.

APPENDIX A

PI-PDMS EXPEREIEMENT WITH NARROWED CHANNEL DIMENSION

Materials and methods

In order to narrow down the size of the channels, we redesign the shims and the microfluidic device. The new design of the device is made of aluminum plates with steel stainless shims. This device was constructed to enable high temperature experiments in the future, although here we will only discuss experiments at room temperature. Here the liquid-liquid experiment of Chapter 5 was repeated to test whether we can reliably generate drops with a downstream breakup when the filament diameter is small. The shims were designed in different channels with the laser machining. The design drawings are listing below (Figure 48, Figure 49).

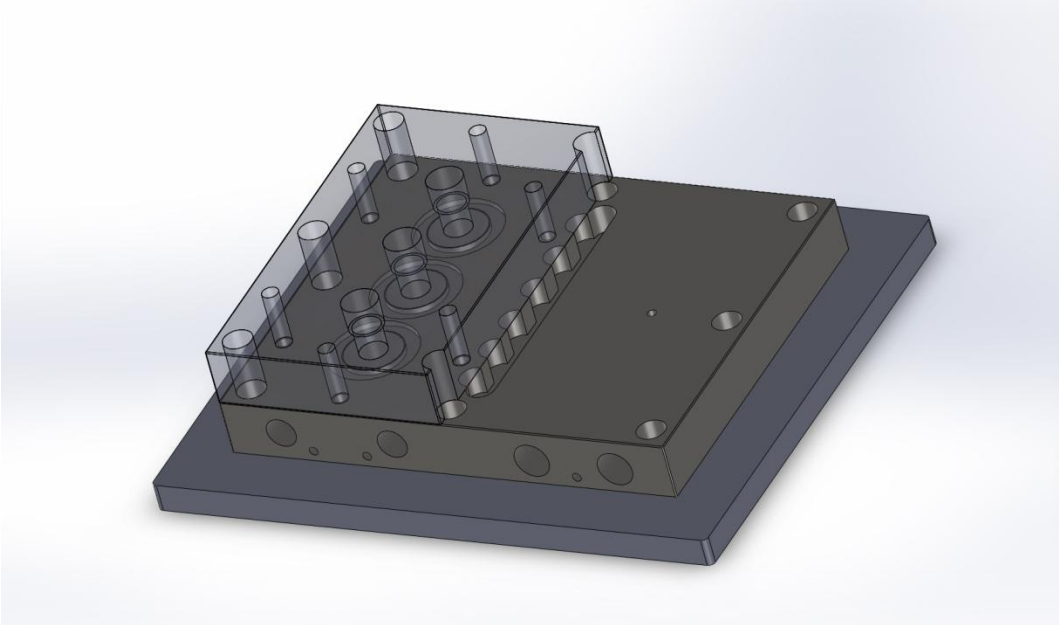

Figure 48 The high temperature microfluidid device. All components shown are made of metal, not acrylic as in Figure 7.

The geometry was similar to that used in the rest of the thesis except that the widths of the main channels were 150 μm, and the constriction (75 μm) in the intersection as will be shown in Figure 49. Furthermore, due to the smaller dimensions of the channels, the pressures required to drive flow were higher and hence conventional dial gauges were used to measure the applied pressure. The rest of the experiment setup was as same as before. PI was used as the dispersed phase and PDMS 100K liquids with various viscosities were used as the continuous phase. The experiment procedure are remained the same as before; the P_c value was kept fixed and P_d was increased gradually to identify the range of P_d values in which droplet formation was evident. P_d here is set up a fixed value 32 psi.

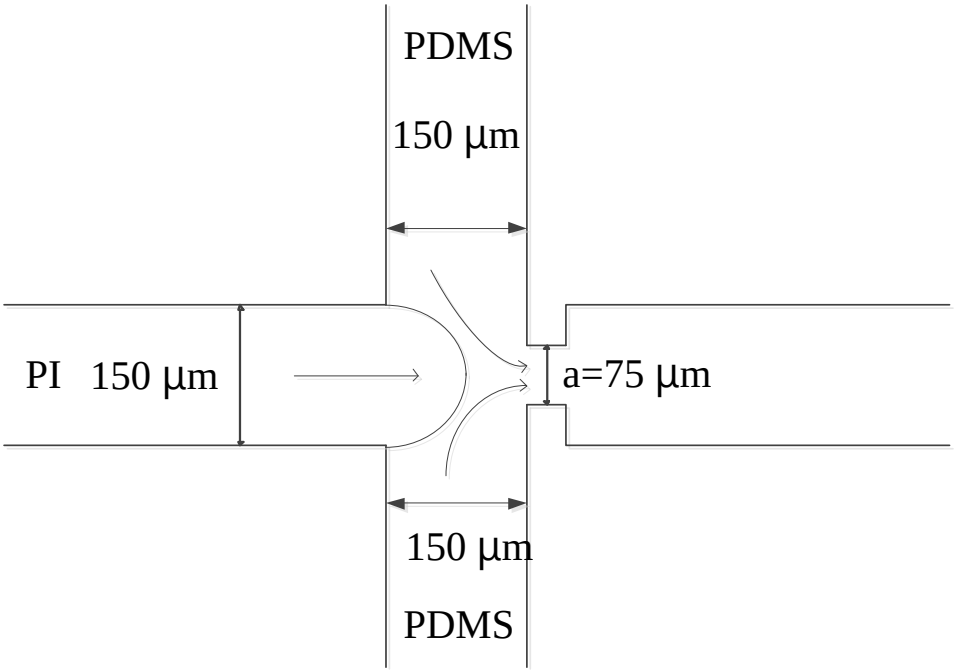

Figure 49 Geometry of the cross flow junction along with dimensions.

Results

The results of the experiments were similar; the dispersed phase PI was found to form a continuous filament, rather than breakup into drops in the intersection. After the intersection, because of the instability of the stream, the stream broke up into droplets in the downstream shown in the Figure 50. The drop sizes increased with increasing P_d, as shown in the Figure 51. Figure 52 shows the diameter changes of the thread sizes with the P_d increased.

Clearly in these cases, the diameter of the filament was much smaller than obtained in Chapter 5 and downstream breakup was observed in all these experiments. Moreover, the point at which capillary breakup occurred (as measured from the junction) increased with increasing P_d.

This may be because the thicker filaments generated at higher P_d take a longer time to break. Finally, the frequency shown in the Figure 54 decreased with the increase of the P_d.

In the Chapter 5, we found that the thread size is an important factor to form jetting phenomenon. We tried to accelerate the capillary instability by perturbing the stream, but this did not affect the stability of the filament noticeably. In contrast, here we note that in the narrower micro-channel, downstream capillary breakup occurs readily and drops that are less than 40 microns in diameter can be realized readily.

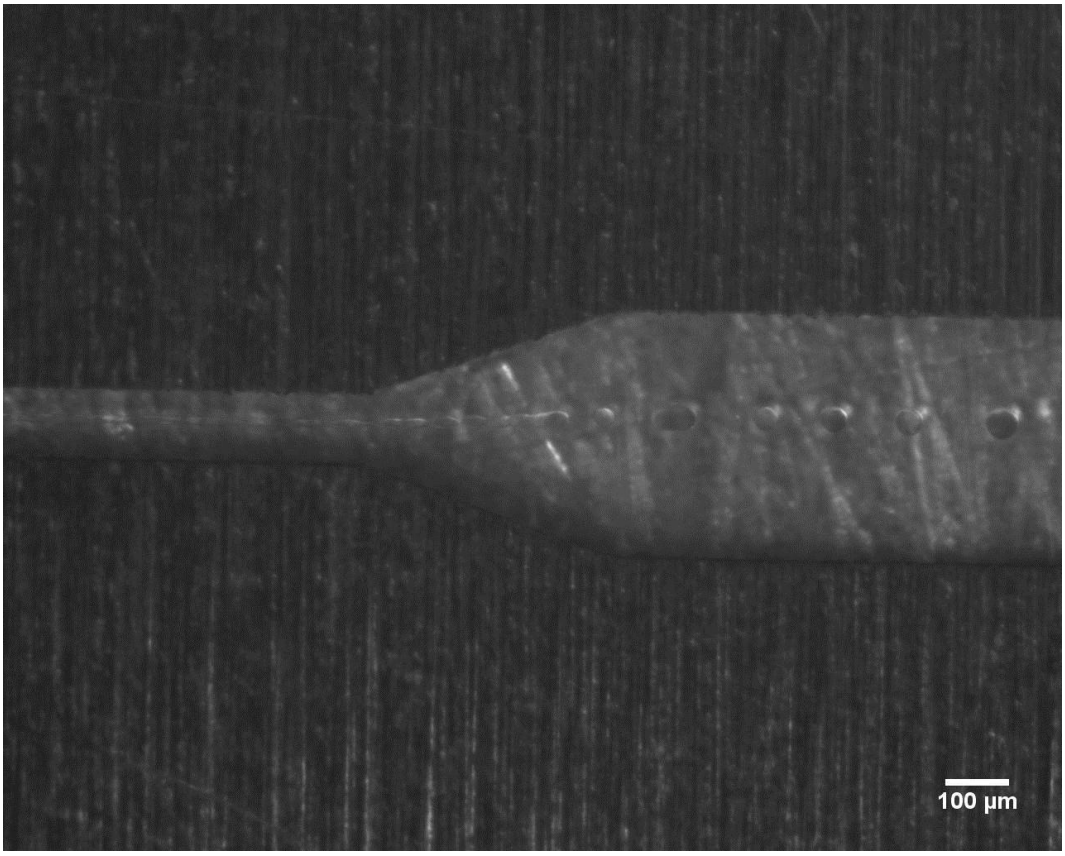

Figure 50 Drop formation by downstream capillary breakup. The continuous phase fluid here is PDMS 100K, and the dispersed phase fluid is PI. P_c here is 32 psi, P_d is 28 psi.

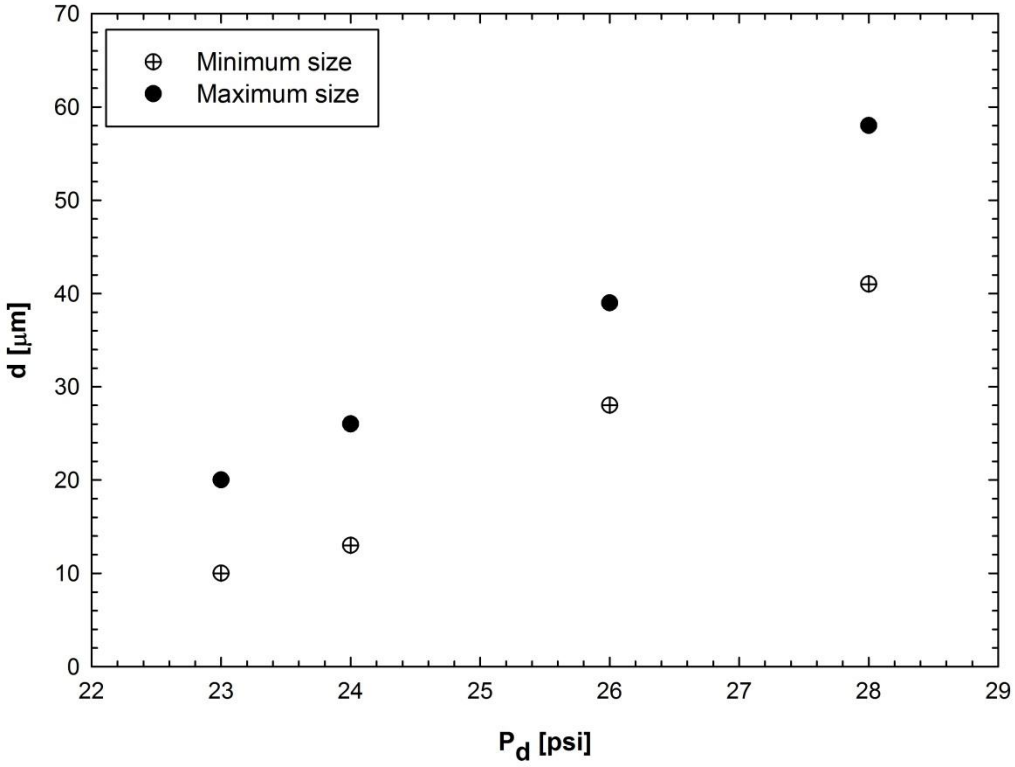

Figure 51 Dependence of drop size on P_d when P_c value was kept fixed at 32 psi.

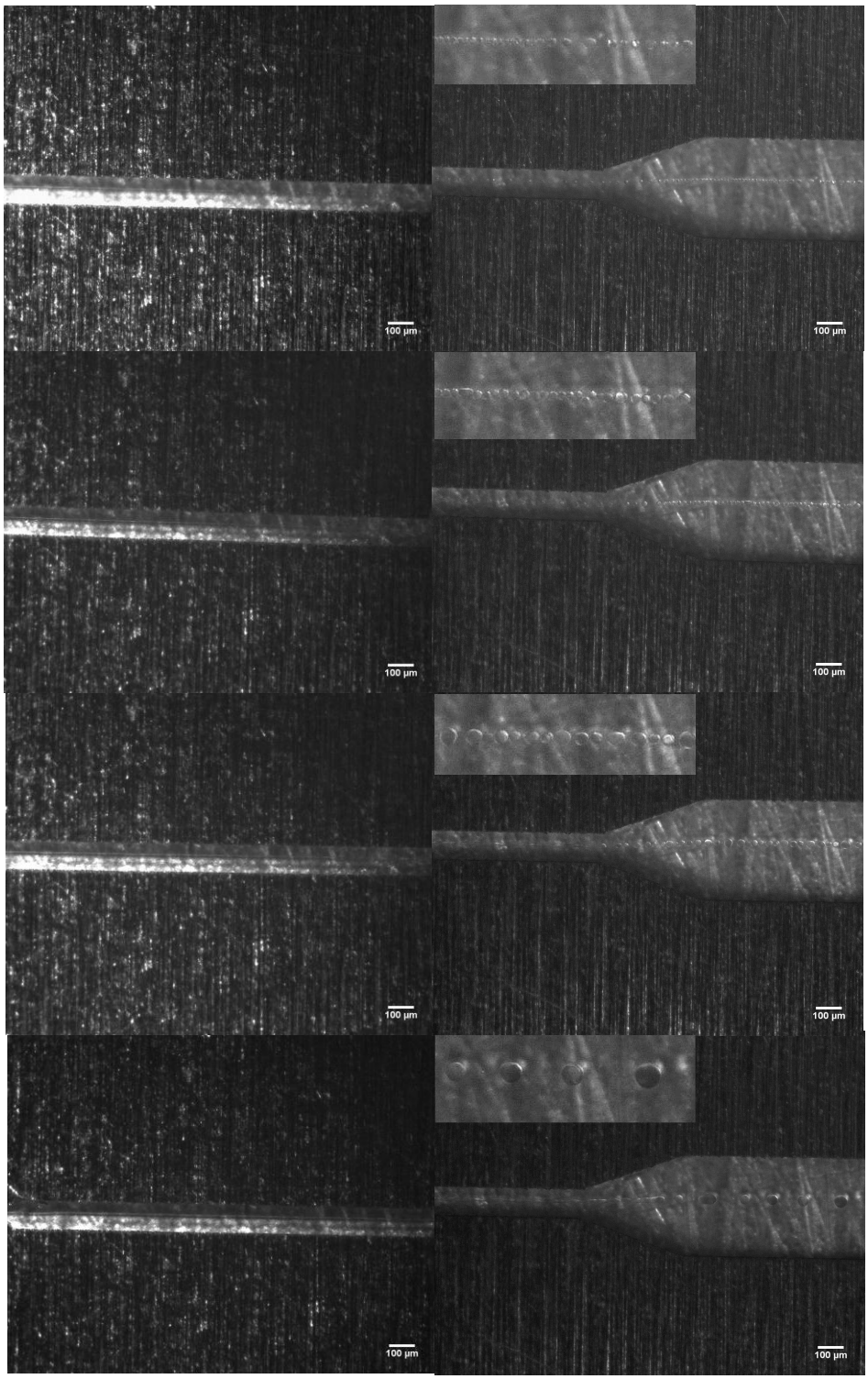

Figure 52 The thread diameter changed with P_d.

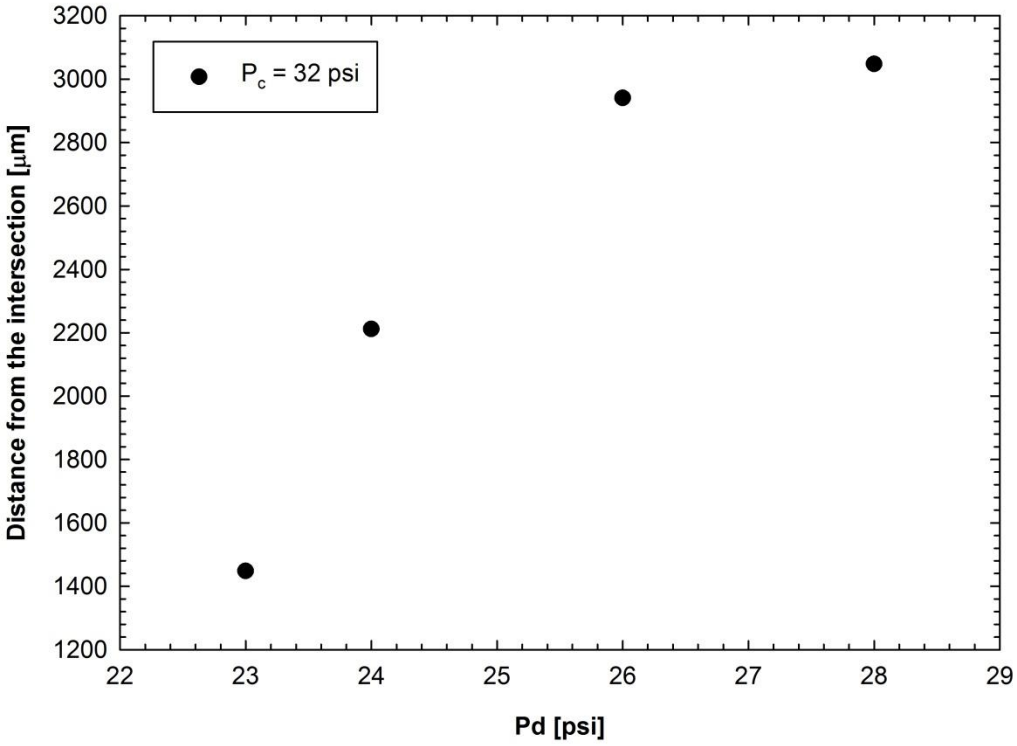

Figure 53 The distance of the point of the break up from the intersection depended on the $P_{d.}$

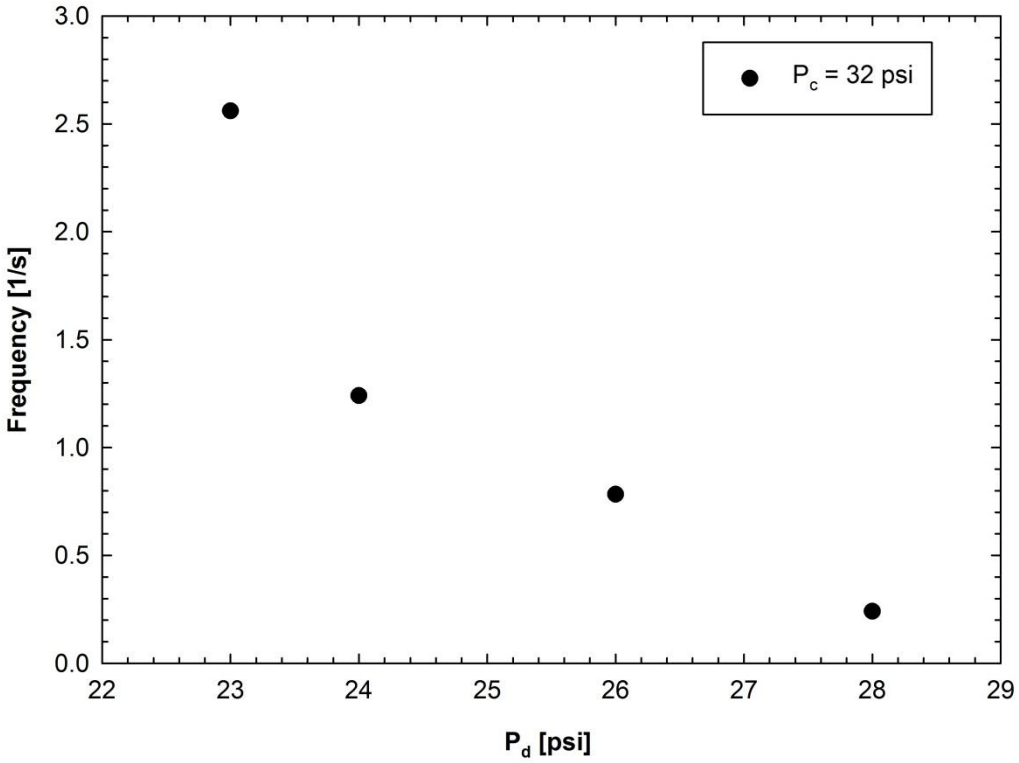

Figure 54 Frequency of the downstream breakup droplets dependence on $P_{d.}$

BIBLIOGRAPHY

1. Stone, H.A., A.D. Stroock, and A. Ajdari, *Engineering flows in small devices: Microfluidics toward a lab-on-a-chip.* Annual Review of Fluid Mechanics, 2004. **36**: p. 381-411.

2. Whitesides, G.M., *The origins and the future of microfluidics.* Nature, 2006. **442**(7101): p. 368-373.

3. Terry, S.C., J.H. Jerman, and J.B. Angell, *A gas chromatographic air analyzer fabricated on a silicon wafer.* Electron Devices, IEEE Transactions on, 1979. **26**(12): p. 1880-1886.

4. Kenis, P.J.A., R.F. Ismagilov, and G.M. Whitesides, *Microfabrication Inside Capillaries Using Multiphase Laminar Flow Patterning.* Science, 1999. **285**(5424): p. 83-85.

5. Thorsen, T., et al., *Dynamic pattern formation in a vesicle-generating microfluidic device.* Physical Review Letters, 2001. **86**(18): p. 4163-6.

6. Sugiura, S., et al., *Preparation of Monodispersed Solid Lipid Microspheres Using a Microchannel Emulsification Technique.* Journal of Colloid and Interface Science, 2000. **227**(1): p. 95-103.

7. Zheng, H.J., et al., *Comparison of Dot-Elisa with Sandwich Elisa in Detecting Circulating Antigen in Patients with Bancroftian Filariasis.* Chinese Medical Journal, 1990. **103**(9): p. 709-712.

8. Leng, S.X., et al., *ELISA and multiplex technologies for cytokine measurement in inflammation and aging research.* Journals of Gerontology Series a-Biological Sciences and Medical Sciences, 2008. **63**(8): p. 879-884.

9. Diercks, A.H., et al., *A microfluidic device for multiplexed protein detection in nano-liter volumes.* Analytical Biochemistry, 2009. **386**(1): p. 30-35.

10. Nie, Z.H., et al., *Janus and ternary particles generated by microfluidic synthesis: Design, synthesis, and self-assembly.* Journal of the American Chemical Society, 2006. **128**(29): p. 9408-9412.

11. Shive, M.S. and J.M. Anderson, *Biodegradation and biocompatibility of PLA and PLGA microspheres.* Adv Drug Deliv Rev, 1997. **28**(1): p. 5-24.

12. Dendukuri, D. and P.S. Doyle, *The Synthesis and Assembly of Polymeric Microparticles Using Microfluidics.* Advanced Materials, 2009. **21**(41): p. 4071-4086.

13. Xu, S., et al., *Generation of monodisperse particles by using microfluidics: Control over size, shape, and composition (vol 44, pg 724, 2005).* Angewandte Chemie-International Edition, 2005. **44**(25): p. 3799-3799.

14. Hwang, D.K., D. Dendukuri, and P.S. Doyle, *Microfluidic-based synthesis of non-spherical magnetic hydrogel microparticles.* Lab on a Chip, 2008. **8**(10): p. 1640-1647.

15. Li, W., et al., *Multi-Step Microfluidic Polymerization Reactions Conducted in Droplets: The Internal Trigger Approach.* Journal of the American Chemical Society, 2008. **130**(30): p. 9935-9941.

16. Pregibon, D.C., M. Toner, and P.S. Doyle, *Multifunctional encoded particles for high-throughput biomolecule analysis.* Science, 2007. **315**(5817): p. 1393-1396.

17. Sugiura, S., et al., *Size control of calcium alginate beads containing living cells using micro-nozzle array.* Biomaterials, 2005. **26**(16): p. 3327-3331.

18. Khan, S.A. and K.F. Jensen, *Microfluidic synthesis of titania shells on colloidal silica.* Advanced Materials, 2007. **19**(18): p. 2556-+.

19. Shepherd, R.F., et al., *Stop-Flow Lithography of Colloidal, Glass, and Silicon Microcomponents.* Advanced Materials, 2008. **20**(24): p. 4734-+.

20. Sung, K.E., et al., *Programmable fluidic production of microparticles with configurable anisotropy.* Journal of the American Chemical Society, 2008. **130**(4): p. 1335-1340.

21. Nisisako, T., T. Torii, and T. Higuchi, *Droplet formation in a microchannel network.* Lab on a Chip, 2002. **2**(1): p. 24-26.

22. van der Graaf, S., et al., *Droplet formation in a T-shaped microchannel junction: A model system for membrane emulsification.* Colloids and Surfaces A: Physicochemical and Engineering Aspects, 2005. **266**(1–3): p. 106-116.

23. Xu, J.H., et al., *Formation of monodisperse microbubbles in a microfluidic device.* AIChE Journal, 2006. **52**(6): p. 2254-2259.

24. Garstecki, P., et al., *Formation of droplets and bubbles in a microfluidic T-junction-scaling and mechanism of break-up.* Lab on a Chip, 2006. **6**(3): p. 437-446.

25. Guillot, P. and A. Colin, *Stability of parallel flows in a microchannel after a T junction.* Physical Review E, 2005. **72**(6): p. 066301.

26. Anna, S.L., N. Bontoux, and H.A. Stone, *Formation of dispersions using "flow focusing" in microchannels.* Applied Physics Letters, 2003. **82**(3): p. 364-366.

27. Xu, Q. and M. Nakajima, *The generation of highly monodisperse droplets through the breakup of hydrodynamically focused microthread in a microfluidic device.* Applied Physics Letters, 2004. **85**(17): p. 3726-3728.

28. Yobas, L., et al., *High-performance flow-focusing geometry for spontaneous generation of monodispersed droplets.* Lab on a Chip, 2006. **6**(8): p. 1073-1079.

29. Hamlington, B.D., et al., *Liquid crystal droplet production in a microfluidic device.* Liquid Crystals, 2007. **34**(7): p. 861-870.

30. Gañán-Calvo, A.M., *Perfectly monodisperse microbubbling by capillary flow focusing: An alternate physical description and universal scaling.* Physical Review E, 2004. **69**(2): p. 027301.

31. Utada, A.S., et al., *Monodisperse Double Emulsions Generated from a Microcapillary Device.* Science, 2005. **308**(5721): p. 537-541.

32. Cramer, C., P. Fischer, and E.J. Windhab, *Drop formation in a co-flowing ambient fluid.* Chemical Engineering Science, 2004. **59**(15): p. 3045-3058.

33. Hong, Y. and F. Wang, *Flow rate effect on droplet control in a co-flowing microfluidic device.* Microfluidics and Nanofluidics, 2007. **3**(3): p. 341-346.

34. Hua, J., B. Zhang, and J. Lou, *Numerical simulation of microdroplet formation in coflowing immiscible liquids.* AIChE Journal, 2007. **53**(10): p. 2534-2548.

35. Utada, A.S., et al., *Dripping to Jetting Transitions in Coflowing Liquid Streams.* Physical Review Letters, 2007. **99**(9): p. 094502.

36. Umbanhowar, P.B., V. Prasad, and D.A. Weitz, *Monodisperse emulsion generation via drop break off in a coflowing stream.* Langmuir, 2000. **16**(2): p. 347-351.

37. Cubaud, T. and T.G. Mason, *Capillary threads and viscous droplets in square microchannels.* Physics of Fluids, 2008. **20**(5).

38. Moon, D., A.J. Bur, and K.B. Migler, *Multi-sample micro-slit rheometry.* Journal of Rheology, 2008. **52**(5): p. 1131-1142.

39. Ward, T., et al., *Microfluidic flow focusing: Drop size and scaling in pressure versus flow-rate-driven pumping.* Electrophoresis, 2005. **26**(19): p. 3716-3724.

40. Bong, K.W., et al., *Compressed-air flow control system.* Lab on a Chip, 2011. **11**(4): p. 743-747.

41. Ho, B.P. and L.G. Leal, *The creeping motion of liquid drops through a circular tube of comparable diameter.* Journal of Fluid Mechanics, 1975. **71**(02): p. 361-383.

42. Dietrich, N., et al., *Bubble Formation Dynamics in Various Flow-Focusing Microdevices.* Langmuir, 2008. **24**(24): p. 13904-13911.

43. Mortensen, N.A., F. Okkels, and H. Bruus, *Reexamination of Hagen-Poiseuille flow: Shape dependence of the hydraulic resistance in microchannels.* Physical Review E, 2005. **71**(5): p. 057301.

44. Anna, S.L. and H.C. Mayer, *Microscale tipstreaming in a microfluidic flow focusing device.* Physics Of Fluids, 2006. **18**(12).

45. Nie, Z.H., et al., *Emulsification in a microfluidic flow-focusing device: effect of the viscosities of the liquids.* Microfluidics and Nanofluidics, 2008. **5**(5): p. 585-594.

46. Thareja, P. and S. Velankar, *Interfacial activity of particles at PI/PDMS and PI/PIB interfaces: analysis based on Girifalco–Good theory.* Colloid & Polymer Science, 2008. **286**(11): p. 1257-1264.

47. De Menech, M., et al., *Transition from squeezing to dripping in a microfluidic T-shaped junction.* Journal of Fluid Mechanics, 2008. **595**: p. 141-161.